Search for Large Extra Dimensions in the Diphoton Final State at the Large Hadron Collider

by

Duong Nguyen

M.Sc., University of Natural Sciences; Ho Chi Minh City, Vietnam, 2004

B.Sc., University of Natural Sciences; Ho Chi Minh City, Vietnam, 2000

A dissertation submitted in partial fulfillment of the
requirements for the degree of Doctor of Philosophy
in The Department of Physics at Brown University

PROVIDENCE, RHODE ISLAND

May 2011

This dissertation by Duong Nguyen is accepted in its present form
by The Department of Physics as satisfying the
dissertation requirement for the degree of Doctor of Philosophy.

Date_____ _____

Professor Greg Landsberg, Advisor

Recommended to the Graduate Council

Date_____ _____

Professor Chung-I Tan, Reader

Date_____ _____

Professor David Cutts, Reader

Approved by the Graduate Council

Date_____ _____

Peter M. Weber, Dean of the Graduate School

Acknowledgements

It is my pleasure to thank the many people who made this dissertation possible.

First of all, I would like to express my deep and sincere gratitude to my advisor, Professor Greg Landsberg. I thank him for his great guidance, assistance, stimulating suggestions, and encouragement during these years of my research. His patience, flexibility, and belief in me have boosted my confidence to become an independent researcher.

Next, I would like to thank my Brown University's group for providing such a wonderful working environment and for being so supportive to me during these years. It was really a pleasure to be a part of the group. My special thanks to John Paul Chou for all his help, for always being kind to answer all sorts of questions and giving me valuable suggestions on my dissertation.

I am also grateful to my committee members, Professor David Cutts and Professor Chung-I Tan for spending their time to read my thesis and give me their valuable advice and suggestions.

My special thanks to Quyen Nguyen and Vietnamese friends at Brown University for their constant support and friendship.

Last but not least, to my parents and my little family, I owe the biggest debt of

gratitude. Without their unconditional love and consistent support over the years, I would never have gotten this far.

Abstract of " Search for Large Extra Dimensions in the Diphoton Final State at the Large Hadron Collider " by Duong Nguyen, Ph.D., Brown University, May 2011

We performed a search for large extra spatial dimensions via virtual graviton exchange in the diphoton channel with the Compact Muon Solenoid detector at the Large Hadron Collider. No excess of events above the Standard Model predictions has been found using a data sample collected in proton-proton collisions at the $\sqrt{s} = 7$ TeV and corresponding to an integrated luminosity of approximately 36 pb^{-1}. New limits are set on the effective Planck scale in the range of 1.6–2.3 TeV, at the 95% confidence level, depending on the number of extra dimensions. These are the most restrictive bounds on models with more than two large extra dimensions to date.

Contents

List of Tables

List of Figures

Chapter 1

Introduction

For nearly forty years, the Standard Model (SM) has proven to be a very successful theory framework in particle physics. Its phenomenological predictions have been confirmed by a variety of measurements up-to the TeV scale at fixed target, lepton and hadron collider experiments. However, there are many unanswered questions in the theoretical construction of the SM that make us believe that the SM is an incomplete model. Furthermore, the existence of two fundamental scales that are so different from each other results in the so-called hierarchy problem. This has led to the idea of extending our 3+1 space-time dimensions to include additional compactified large extra dimensions. This dissertation presents a search for the existence of these extra dimensions at the Large Hadron Collider.

We begin this chapter with an overview of the SM and its history. After that, we describe the hierarchy problem and one of its solutions, the Large Extra Dimension paradigm. Finally, we review results from different experimental searches for large extra dimensions.

1.1 The Standard Model of High Energy Physics

The Standard Model of high energy physics is a relativistic quantum field theory describing the interactions between fundamental particles. There are four known types of interactions: gravitational, electromagnetic, weak and strong (but gravity is not included in the SM). The interactions between leptons and quarks are carried out via spin-1 (vector) gauge bosons: γ, W, Z and gluon. The electromagnetic (γ) and weak (W, Z) interactions are unified and described in a common framework called the electroweak theory.

Leptons and quarks are fermions and are organized in 3 generations. The question why there are three generations can not be answered within the Standard Model itself. The photon, W and Z bosons, and gluons are responsible for transmitting the electromagnetic, weak and strong interactions, respectively. Although the quantum treatment of gravity is incomplete, the massless spin-2 graviton is considered the gauge boson of the gravitational field and transmits the gravitational force. The gravitational attraction is very small for microscopic particles compared to other forces (10^{-29} weaker than the weak force). Therefore, it is usually ignored when considering interactions between particles. However, its tiny strength raises a question about the naturalness of the theoretical construction. This is referred as the hierarchy problem of the SM.

Table 1.1 lists SM particles with six leptons and six quarks arranged in a 3-generation structure. Beside the electric charge, quarks have an additional degree of freedom called the color charge which is red (r), blue (b) or green (g). Note that for each particle, there is partner anti-particle which has the same mass, but opposite electric and color charges.

Generation	Particle	Mass	Charge
	Leptons		
1	Electron (e)	0.5110 MeV/c^2	-1
1	Electron neutrino (ν_e)	< 2 eV	0
2	Muon (μ)	105.7 MeV/c^2	-1
2	Muon neutrino (ν_μ)	< 0.19 MeV	0
3	Tau (τ)	1776.82 ± 0.16 MeV/c^2	-1
3	Tau neutrino (ν_τ)	< 18.2 MeV	0
	Quarks		
1	Up (u)	1.7-3.3 MeV/c^2	2/3
1	Down (d)	4.1-5.8 MeV/c^2	-1/3
2	Charm (c)	$1.27^{+0.07}_{-0.09}$ GeV/c^2	2/3
2	Strange (s)	101^{+29}_{-21} MeV/c^2	-1/3
3	Top (t)	$172.0 \pm 0.9 \pm 1.3$ GeV/c^2	2/3
3	Bottom (b)	$4.19^{+0.18}_{-0.06}$ GeV/c^2	-1/3

Table 1.1: Standard Model particles [1].

The interactions between fundamental particles of the SM can be described by a Lagrangian. In order for the theory to be renormalizable, the Lagrangian is required to be invariant under local gauge transformations. The local gauge transformation belongs to a gauge symmetry group. The SM dynamical properties are described by the $SU(3)_C \otimes SU(2)_L \otimes U(1)_Y$ gauge group structure, where C denotes the color charge, L implies that SU(2) acts on the left-handed fields, and Y is the weak hypercharge which relates to electric charge Q and the third component of the weak isospin T_3 by the equation, $Y = 2(Q - T_3)$. The electroweak interaction is described by the $SU(2)_L \otimes U(1)_Y$ sector while the strong interaction is described by the $SU(3)$ gauge transformation group.

The local gauge invariant requirement on the Lagrangian introduces new fields and their associated spin-1 gauge bosons. For the SU(2) gauge transformation, the gauge fields are W^i_μ, i = 1,..,3. The gauge field corresponding to the U(1) transformation is B_μ. The $W^{1,2}_\mu$ gauge fields are combined to form the charge states

W_μ^+, W_μ^-, which are identified as the physical $W^\pm$ bosons, according to

$$W_\mu^\pm = \frac{-W_\mu^1 \pm iW_\mu^2}{\sqrt{2}}, \tag{1.1}$$

$$W_\mu^0 = W_\mu^3. \tag{1.2}$$

The unification of the electromagnetic and weak interactions following the $SU(2) \otimes U(1)$ gauge group is expressed in the combination of B_μ and W_μ^3:

$$A_\mu = \frac{g_2 B_\mu - g_1 Y_L W_\mu^3}{\sqrt{g_2^2 + g_1^2 Y_L^2}}, \tag{1.3}$$

$$Z_\mu = \frac{g_1 Y_L B_\mu + g_2 W_\mu^3}{\sqrt{g_2^2 + g_1^2 Y_L^2}}, \tag{1.4}$$

where Y_L is the left-handed projection of the hypercharge Y, for which $Y_L = -1$, g_1 and g_2 are the coupling constants of the U(1) and SU(2) fields, A_μ and Z_μ correspond to massless photon and neutral boson Z, respectively. Defining $sin\theta_w = g_1/\sqrt{g_1^2 + g_2^2}$, where θ_w is the Weinberg angle ($sin^2\theta_w \sim 0.23$), we have:

$$g_1 = \frac{e}{cos\theta_w}, \qquad g_2 = \frac{e}{sin\theta_w}, \qquad g_Z = \frac{e}{sin\theta_w cos\theta_w}; \tag{1.5}$$

$$A_\mu = W_\mu^3 sin\theta_w - B_\mu cos\theta_w, \quad Z_\mu = W_\mu^3 cos\theta_w + B_\mu sin\theta_w, \tag{1.6}$$

where e is the electromagnetic coupling constant or the electric charge, and g_Z is the coupling constant of the Z_μ field.

Local gauge invariant requires the bosons to be massless. However, experiment measurements exclude this for the W and Z bosons. Therefore, the symmetry is not exact, but it is spontaneously broken by the Higgs mechanism to give masses to the gauges bosons. At the leading order, the SM predicts that $M_W/M_Z = cos\theta_w$.

Quarks and leptons are arranged into left-handed doublets and right-handed

singlets. For example, the first generation lepton doublet is (ν_{eL}, e_L) and the singlet is e_R. There are no right-handed neutrinos in the Standard Model. For leptons, the charge-current weak interaction transmitted by $W^{\pm}$ gives strictly transitions within a generation. For quark doublets, generational mixing occurs for example via (u_L, $d_L^{'}$), where $d_L^{'} = d_L cos\theta_C + s_L sin\theta_C$ and θ_C is the cabbibo angle. Therefore, the charge-changing transitions happen between generations. The neutral-current interaction is transmitted by the Z boson without charge changing. This interaction transmutes the doublet and the singlet members into themselves.

The SU(3) group of local gauge transformation, which changes the color, has eight generators corresponding to eight G_{μ}^{a} fields (a=1,...,8). Therefore, there are eight massless gauge bosons, called the gluons. The strength of strong interaction varies with distance. It is weak at short distances but strong at large distances. This feature is called asymptotic freedom, and it explains why quarks are confined inside hadrons. Furthermore, since gluons carry color, they couple directly to each other. Therefore, calculations in quantum chromodynamic (QCD) theory are very challenging. Table 1.2 summarizes the properties of the gauge bosons of the SM.

Particle	Interaction	Mass (GeV/c^2)	Charge (e)
Photon (γ)	Electromagnetic	0	0
$W^{\pm}$	Weak	80.2	$\pm$1
Z	Weak	91.2	0

Table 1.2: SM gauge bosons.

The SM was developed in 1960s and the early 1970s. Sheldon Glashow proposed the unification of the electromagnetic and the weak forces in 1963 [19]. The Higgs mechanism was incorporated in the electroweak model in 1967 by Steven Weinberg [20] and Abdus Salam [21]. Gerard 't Hooft showed that gauge theories are renormalizable in 1971 [22]. The QCD theory was completed by David Gross,

Frank Wilczek and David Politzer with the discovery of the asymptotic freedom in 1973 [23, 24]. In the same year, Kobayashi and Maskawa proposed three-generation structure of the SM. However, the final missing members of the third generation were observed only recently: in 1995 for the top quark [25, 26] and in 2001 for the tau neutrino [27].

1.2 Hard Scattering Cross Section

The LHC is a proton-proton collider. The proton quantum numbers suggest that protons are the bound state of *uud* valence quarks. They are also composed of radiated gluons and a sea of quark-antiquark pairs. These constituents are called partons. Because the QCD coupling runs with the momentum transfer, or energy scale (Q) of the parton-parton interaction and it is strong at low Q, the perturbative calculations at low Q are invalid. In general, the coupling constant is determined by the β-function at the renormalization group. If one limits the QCD perturbative expansion of this function at the lowest order coefficient, the coupling constant $\alpha_s(Q^2)$ is defined as [4]:

$$\alpha_S(Q^2) = \frac{\alpha_S(\mu^2)}{1 + \frac{33-2n_f}{12\pi}\alpha_S(\mu^2)\ln(\mathrm{Q}^2/\mu^2)}, \tag{1.7}$$

where μ is the renormalization scale at which a subtraction is performed to remove the ultraviolet divergences in the renormalization procedure. This parameter is chosen arbitrarily. A convenient choice is $\mu = M_Z$ which is large enough to be in the perturbative domain. Ref. [28] quotes:

$$\alpha_s(M_Z^2) = 0.1184 \pm 0.0007 \tag{1.8}$$

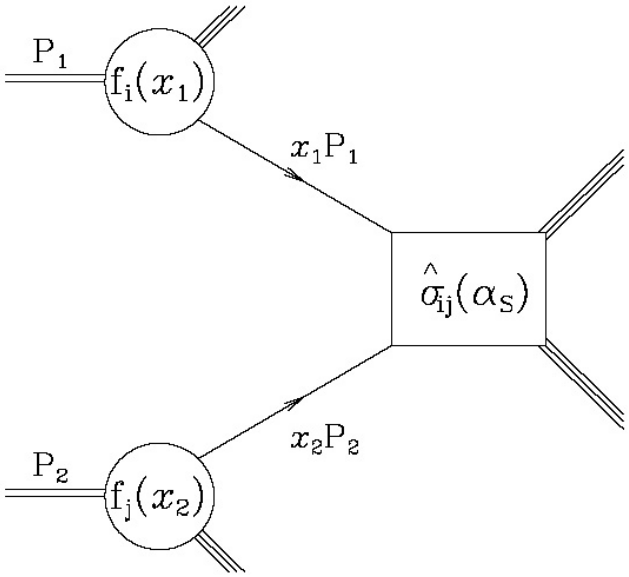

Figure 1.1: The parton model description of a hard scattering process [4].

Historically, a dimensional parameter $\Lambda_{QCD} \sim 200$ MeV is introduced directly in the definition of $\alpha_S(Q^2)$. This is the value where the coupling would diverge. However, this choice has some disadvantages: it is not dimensionless, and it depends on the number of active flavors, n_f, and on the renormalization scheme.

In a hard scattering or high-Q^2 processes, the cross sections are factorized based on the factorization theorem of QCD [29]:

$$\sigma(P_1, P_2) = \sum_{i,j} \int dx_1 dx_2 f_i(x_1, \mu_F^2) f_j(x_2, \mu_F^2) \widehat{\sigma}_{ij}(p_1, p_2, \alpha_S(\mu_R^2), Q^2/\mu_F^2), \qquad (1.9)$$

where P_1, P_2 is the four-momenta of incoming hadrons, $p_1 = x_1 P_1$, $p_2 = x_2 P_2$ are the four-momenta of partons participating in the hard interaction, $f_{i,j}(x, \mu_F^2)$ are the parton (gluon or quark) distribution functions (PDFs) defined at a factorization scale μ_F, and $\widehat{\sigma}_{ij}$ is the short-distance cross section for the scattering of the partons i and j. Because the coupling constant is small at high energy, this cross section is calculated as a perturbation series in the running coupling α_S.

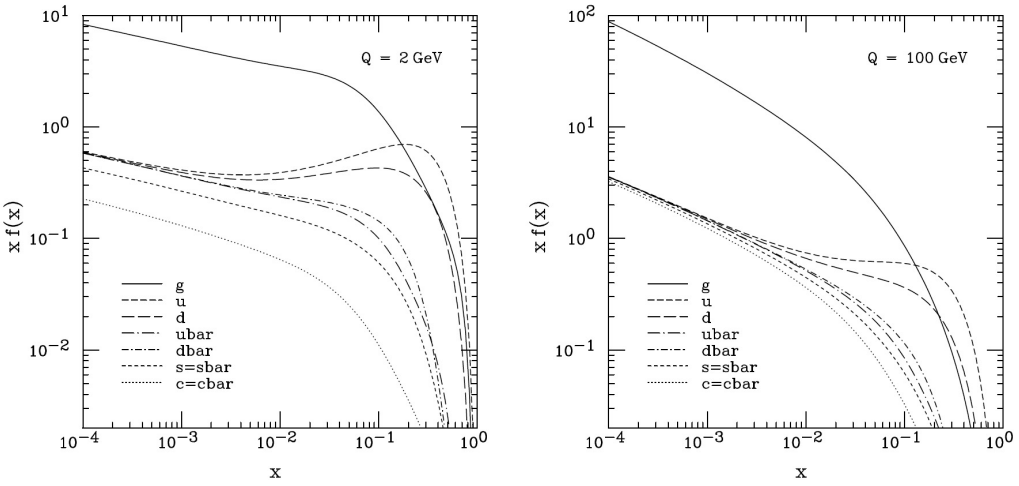

Figure 1.2: The CTEQ6M parton distribution functions at $Q = 2$ and 100 GeV [5].

The factorization factor is an arbitrary parameter which separates the long- and short-distance calculations. If an emitted parton has transverse momentum less than μ_F, it is considered to be a part of the hadron structure and is absorbed into the parton distribution function. In contrast, a high transverse momentum parton is a part of the short-distance cross section. The dependence of cross section on μ_F is weaker if more terms are included in the perturbative expansion.

The PDFs are the probability density to find a parton inside of the proton with a given fraction of the total momentum. It is determined from experimental measurements. An example of these functions are calculated by the CTEQ collaboration based on QCD studies at HERA and the Tevatron. Both the parton distribution functions and short-distance cross section, $\widehat{\sigma}$, depend on the scales. Therefore, the scales need to be used consistently in the PDFs and in the short-distance calculation. Otherwise, cancellation of ultraviolet and collinear divergences does not match. A common setup for the scales is $Q^2 = \mu_R^2 = \mu_F^2$.

1.3 Direct Photon Production

Direct photons are photons produced in the parton-parton collisions, which distinguishes them from photons from the decays of neutral hadrons (for example π^0). A photon is created in association with jets in the Compton process ($qg \rightarrow \gamma q$) or annihilation process ($q\overline{q} \rightarrow \gamma q$). Figure 1.3 shows the leading order ($O(\alpha\alpha_S)$) diagrams in the production cross section calculation, where α and α_S are the electromagnetic and strong couplings, respectively.

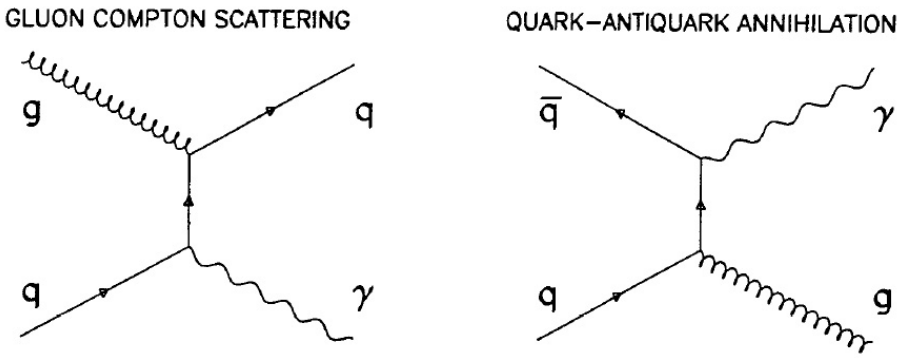

Figure 1.3: Leading order Feynman diagram of gamma+jet process.

Photon pairs are also produced in proton-proton collisions. The LO cross section ($O(\alpha^2)$) comes from the quark-antiquark annihilation ($q\overline{q} \rightarrow \gamma\gamma$). The tree-level diagram is called the Born diagram (diagram a in Figure 1.4). Diagrams d and g in Figure 1.5 show the one- and two- fragment processes where one or both photons come from the collinear fragmentation of hadrons. These diagrams are also at LO. The next-to-leading order diagrams include real (diagram b in Figure 1.4) or virtual (diagram c in Figure 1.4) corrections, which are $O(\alpha_S)$, to the LO Born diagram. Therefore, the total NLO contribution is $O(\alpha^2\alpha_S)$. The corresponding NLO fragmentation processes are shown in Figure 1.5, diagrams e, f, h, i.

There are multiple collinear singularities in the fragmentation diagrams when a

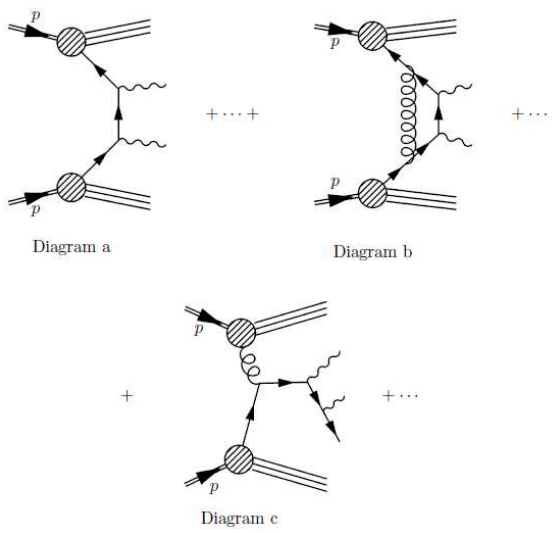

Figure 1.4: The direct contributions to the diphoton cross section. Diagram a: the LO Born process. Diagram b and c: the NLO processes

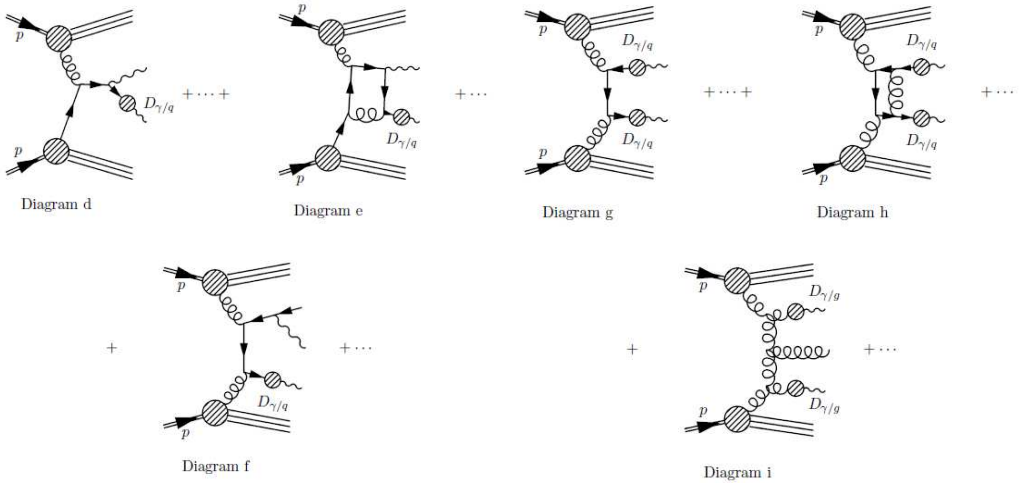

Figure 1.5: The fragmentation contributions to the diphoton cross section. Diagrams d and g: the LO processes. Diagrams e, f, h, i: the corresponding NLO processes. $D_{\gamma/q}$ and $D_{\gamma/g}$ are the fragmentation functions which absorb the quark-photon or gluon-photon singularities

high- p_T parton undergoes a cascade of successive collinear splittings ending up with a parton-photon collinear splitting where the momenta of the photon and parton are nearly parallel. These singularities are absorbed into a photon "fragmentation function" $D_{\gamma/q,g}(z, \mu^2)$ representing the probability of finding a photon carrying a longitudinal momentum fraction z in a quark or gluon jet at a scale μ. If this scale, often chosen at the order of the hard scale of the process, is large compared to any

typical hadronic scale ($\sim$ 1 GeV), these functions have a size of roughly $\alpha/\alpha_S(\mu)$. Therefore, they compensate for the strong interaction vertex contribution, which is $O(\alpha_S)$, in cross section calculation.

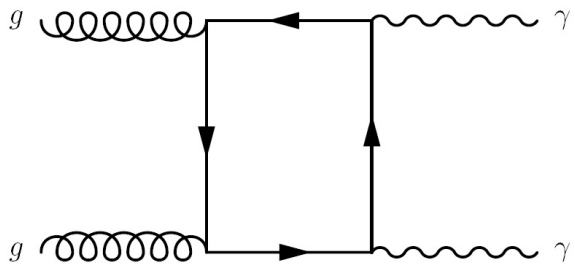

Figure 1.6: The box diagram

Finally, the gluon-gluon fusion process or box diagram at NNLO (next-to-next-to-leading order) is suppressed by $O(\alpha_S^2)$. However, it is often included in the calculations of the cross section at the LHC due to the high gluon luminosity.

1.4 The Hierarchy Problem and Large Extra Dimensions Paradigm

The hierarchy problem refers to the enormous difference between the electroweak symmetry breaking scale, $M_{EWSB} \sim 10^2$ GeV, and the fundamental scale of gravity, $M_{Pl} \sim 10^{19}$ GeV. The consequence of this large difference in scale is that a very high degree of fine-tuning is required to protect the Higgs mass from radiative corrections. For example, the correction for Higgs mass from the fermi on loops (Figure 1.7) is given by:

$$\Delta M_H^2 = \frac{\lambda_f^2}{4\pi^2}(\Lambda^2 + M_H^2) + ..., \tag{1.10}$$

where Λ is the ultraviolet cutoff and λ_f is the self-coupling constant of the Higgs bosons. If Λ is at an order of M_{Pl}, the constraint on the Higgs mass at ∼100 GeV requires the fine-tuning or cancellation of various loops to a precision of $\sim (M_H/\Lambda)^2 \sim 10^{-34}$.

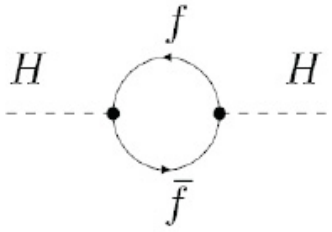

Figure 1.7: The fermion loop correction to Higgs mass

In 1998, Arkani-Hamed, Dimopoulos and Dvali (ADD) proposed the Large Extra Dimensions paradigm to solve the hierarchy problem [30]. In this framework, the SM particles and gauge interactions are constrained to the ordinary 3 + 1 space-time dimensions (SM "brane"), while gravity is free to propagate through the entire multidimensional space (bulk). Therefore, the gravitational force is effectively diluted, and it appears to be weak (strength order $\sim 1/M_{Pl}$) for an observer on the SM brane. For instance, suppose that there are n extra compact spatial dimensions of the same radius ∼R. By applying Gauss's law in (4+n) dimensions, the gravitational potential between two test masses, m_1, m_2 separated by a distance of $r \ll R$ is [30]:

$$V(r) \sim \frac{m_1 \times m_2}{M_D^{n+2}} \frac{1}{r^{n+1}}, (r \ll R), \tag{1.11}$$

where M_D is the fundamental Planck scale of a (4+n) dimensional theory. If two masses are separated by $r \gg R$, their gravitational flux lines can not continue to penetrate in the extra dimensions. Therefore, the potential is:

$$V(r) \sim \frac{m_1 \times m_2}{M_D^{n+2} R^n} \frac{1}{r}, (r \gg R), \tag{1.12}$$

Compared to the Newtonian gravitational potential, the effective M_{Pl} is:

$$M_{Pl}^2 \sim M_D^{n+2} R^n. \tag{1.13}$$

If we set $M_D \sim M_{EW} \sim 1$ TeV, we find that

$$R \sim 10^{\frac{30}{n_{\rm ED}} - 19} \text{m}. \tag{1.14}$$

The $n_{ED} = 1$ case is excluded because R is approximately 10^{11} m, which is on the order of the radius of the Solar system. For $n_{ED} = 2$, $R < 10^{-2}$ cm, which is out of the reach of direct measurements of gravity at short distances [31] (as of 1998, gravitational measurements are not sensitive to the distance smaller than 1 mm). For $n_{ED} = 6$ or 7 (corresponding to the 10 or 11-dimensional space-time suggested by string theory), the size of the extra dimensions is ~ 1 fm, which is large compared to Planck or electroweak lengths; hence, the name Large Extra Dimensions.

The requirement that all particles except gravitons are constrained to the SM brane and must not feel the extra space satisfies constraints from atomic physics and other experimental data. Although the ADD paradigm solves the hierarchy problem by suggesting a fundamental Plank scale of the order of EW scale in the multidimensional space, it converts the energy hierarchy to a distance hierarchy since the size of the extra dimensional space is much larger than the range of EWSB energy scale (about 10^{-19} m). With the existence of extra dimensions, the electroweak scale is the only fundamental scale in nature where the gravitational and gauge interactions unite. Thus, the apparent Planck scale, M_{Pl}, is not the fundamental scale, but its enormity is due to the large size of the new dimensions.

1.5 Searches for Large Extra Dimensions at Colliders

The production of KK gravitons (G_{KK}) at colliders is possible since gravitons couple to the energy-momentum tensor. This implies that graviton can be added to any vertices or lines of SM Feynman diagrams. Because gravitons propagate in the compact extra dimensions, the boundary conditions result in a quantization of the graviton's energy into discrete eigenvalues. From the point of view of a 3-dimensional observer, they look like a tower of graviton excitations, referred to Kaluza–Klein modes. Since the energy spacing between modes is very small ($\sim$ 1 meV-100 MeV given the size of EDs $\sim 10^{-3}$m -10^{-15} m), there are many KK modes to be excited at high energy. Although each KK mode couples to the energy-momentum tensor with the gravitational strength $G_N \sim 1/M_{Pl}^2$, the large number of these modes that can be excited is sufficient to enhance the gravitational coupling tremendously. For example, at the energy of 1 TeV, given the size of ED $\sim$ 1 fm and n_{ED} =7, as many as 10^{28} modes can be excited [32].

One can look for the graviton emission which results in a single jet or a gauge boson associated with a large missing transverse energy due to escapes of gravitons to the extra dimensional space. Direct graviton emissions depend directly on the fundamental Plank scale M_D. However, they are expected to be suppressed by a factor $(\sqrt{\hat{s}}/M_D)^{n_{\rm ED}+2}$, where $\sqrt{\hat{s}}$ is the characteristic center-of-mass energy at which the effects of EDs are most pronounced. Another channel to look for ED effect is the virtual graviton production via Drell-Yan like processes. Subsequently, gravitons decay to two photons or fermions. The later is less sensitive because decays of spin-2 gravitons to spin-1/2 fermions is suppressed. Furthermore, the dependence on the number of extra dimensions for the virtual graviton effects is fairly weak [33, 34]. The

virtual graviton channel is complementary to the direct graviton emission channel because it depends on the ultraviolet cutoff M_S of the KK spectrum. M_S is likely to be lower than M_D, so the extra dimensional effect might be first seen in the virtual graviton channel.

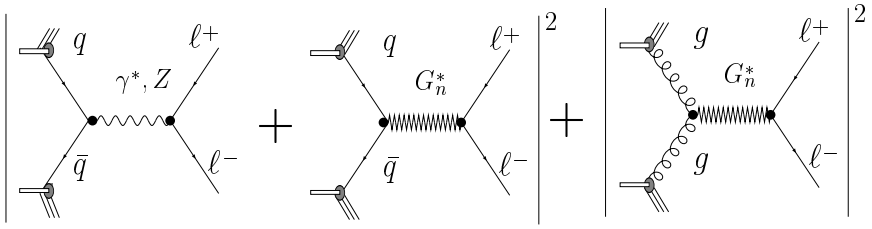

Figure 1.8: DY production Feynman diagrams including the large extra dimensions [6].

The virtual graviton exchange diagrams interfere with their SM counterparts as shown in Figure 1.8 for the DY production. The consequence of additional contributions from these diagrams is an enhancement in DY or diboson spectrum at high invariant masses. The cross section of virtual graviton exchange is not well-defined since it depends on a particular representation of the interaction Lagrangian and the definition of the ultraviolet cutoff for the KK modes. There are three such popular representations [33, 34, 35]. All of them use a variable $\eta_G = \mathcal{F}/M_S^4$, where $\mathcal{F}$ is a dimensionless parameter, and M_S is the ultraviolet cutoff, to parameterize the total or differential cross section with contribution from the G_{KK} exchange:

$$\sigma_{\text{tot}} = \sigma_{\text{SM}} + \eta_G \sigma_{\text{int}} + \eta_G^2 \sigma_G, \tag{1.15}$$

where σ_{SM} is the SM cross section, σ_{int} is the interference term and σ_G is the pure gravitational effect term. Note that, since the G_{KK} exchange effect is expressed by the parameter η_G, which has the dimension of L^4, the interference term, σ_{int} and the pure gravitational effect term, σ_G, have the dimension of L^{-2} and L^{-6}, respectively. L denotes for length.

The parameter $\mathcal{F}$ contains the dependence of the virtual G_{KK} exchange effect on the number of extra dimensions. These definitions used in each representation mentioned above are as follows:

$$\mathcal{F} = 1, \text{ (GRW [33])}; \tag{1.16}$$

$$\mathcal{F} = \begin{cases} \log\left(\frac{M_S^2}{M^2}\right), & n = 2 \\ \frac{2}{n-2}, & n > 2 \end{cases}, \text{ (HLZ [35])}; \tag{1.17}$$

$$\mathcal{F} = \frac{2\lambda}{\pi} = \pm\frac{2}{\pi}, \text{ (Hewett [34])}. \tag{1.18}$$

In the above formula, $\mathcal{F}$ depends explicitly on the number of EDs only in the HLZ formalism. The gravitational effect contributes constructively in both the HLZ and GRW formalism. However, the sign of $\mathcal{F}$ is unknown and included is a parameter λ in the Hewett convention. The value of λ is of order 1 and usually assigned either $+1$ (constructive interference) or -1 (destructive interference).

1.6 Current Constraints and Limits

Searches for extra dimensions have been performed by many experiments and the model parameters are also constrained by astrophysical observations and cosmology. One of the most straightforward approaches is to measure the gravity directly at short distances and look for a modification of Newton's gravitational law. This modification is parameterized by the Yukawa potential,

$$V(r) = -G\frac{m_1 m_2}{r}\left(1 + \alpha e^{-r/\lambda}\right). \tag{1.19}$$

These measurements are sensitive to distances $\sim 50\mu$m with the current techniques. If all extra dimensions have the same sizes, this limit implies that these measurements can not probe $n > 2$ case. However, only the total volume of extra dimensions is important, not the shape of extra dimensions. Therefore, one of extra dimensions might be macroscopic and sensitive to direct measurements probing $n > 2$ cases. The best upper limit on the size of extra dimensions is given by the Eöt-Washington group [36], which is $R < 0.44\ \mu m$ at 95% CL. This limit corresponds to $M_D > 3.2$ TeV for two extra dimensions of equal sizes [7].

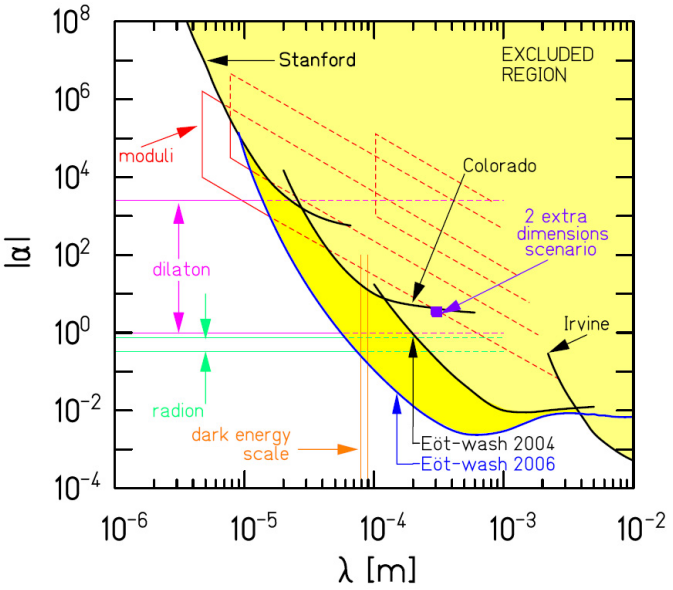

Figure 1.9: Constraints on Yukawa violations of the gravitational $1/r^2$ law. The shaded region is excluded at the 95% confidence level [7].

An example of constraining ADD model using astrophysical observations comes from the observation of a handful of neutrinos from the SN1987A explosion by IMB and Kamiokande detectors. This method is based on the assumption that KK-graviton emission is a competitive cooling mechanism for the supernovae; thus neutrino emission is suppressed. The constraints on M_D found are $M_D > 25 - 30$ GeV for $n = 2$ and 2-4 TeV for $n = 3$ and below 1 TeV for any higher number of extra di-

Table 1.3: 95% CL lower limits on the fundamental Planck scale M_D (in TeV) form Tevatron experiments [2].

Experiment and channel	$n=2$	$n=3$	$n=4$	$n=5$	$n=6$
LEP Combined [38]	1.60	1.20	0.94	0.77	0.66
CDF monophotons [39], 2.0 fb^{-1}	1.08	1.00	0.97	0.93	0.90
DØ monophotons [40], 2.7 fb^{-1}	0.97	0.90	0.87	0.85	0.83
CDF monojets [41], 1.1 fb^{-1}	1.31	1.08	0.98	0.91	0.88
CDF combined [39]	1.42	1.16	1.06	0.99	0.95

Table 1.4: Recent 95% CL lower limits on the ultraviolet cutoff M_S (in TeV) from the Tevatron experiments [2].

DØ Signature	GRW	HLZ				
		n=2	n=3	n=4	n=5	n=6	n=7
$ee+\gamma\gamma$, 1.1 fb^{-1} [42]	1.62	2.09	1.94	1.62	1.46	1.36	1.29
Dijets, 0.7 fb^{-1} [43]	1.56		1.85	1.56	1.41	1.31	1.24

mensions [37]. In general, the limits from astrophysical observations and cosmology are strong (up to 1700 TeV) for $n = 2$, moderate (few TeV) for $n = 3$, and rather weak for $n > 3$ [32]. The uncertainties in predictions are large due to typically high uncertainties of the astrophysical measurements and calculations.

At colliders, LEP experiments searched for extra dimension in both direct graviton emission channel via $e^+e^- \rightarrow \gamma/Z + G_{\rm KK}$ and virtual graviton production via fermions or diboson channels. However, the $e^+e^- \rightarrow \gamma + G_{\rm KK}$ and the $e^+e^- \rightarrow e^+e^-/\gamma\gamma$ channels are the most sensitive. The D0 and CDF collaborations also searched for a gravitational effect in virtual graviton production, monojet and monophotons channels. The most recent 95% limits using 1-3 fb^{-1} data from those searches are presented in Table 1.4. CDF gives the most stringent limits on M_D in the combined monojet and monophoton channel. The best M_S limits comes from D0 using the combined $ee+\gamma\gamma$ channel. D0 also performed for the first time the search in the dijet channel.

Chapter 2

Experimental Apparatus

The Large Hadron Collider (LHC) is the highest energy hadron collider to date, which collides proton beams at a design center-of-mass energy of 14 TeV. In 2010, when the analysis presented in this dissertation was carried out, the center-of-mass energy of the proton-proton collisions was 7 TeV. The Compact Muon Solenoid (CMS) detector, located at collision Point 5 along the LHC ring, measures the outcomes of the collisions. The data collected by CMS are used in a search for large extra dimensions presented in this dissertation. The LHC accelerator complex and the CMS detector are described in Sections 2.1 and 2.2, respectively.

2.1 The Large Hadron Collider

The LHC is a hadron accelerator complex located at the European Organization for Nuclear Research (CERN), Switzerland [3, 8]. It is designed to accelerate proton or heavy ion beams using two main circular acceleration rings with a circumference

of 27 km inside the LEP (Large Electron Positron) tunnel. In order to reach the design collision center-of-mass energy, 14 TeV, the proton beams are accelerated through subsequent steps as shown in Figure 2.1. The proton beams are injected into the Proton Synchrotron (PS) from the linear accelerator and accelerated to 25 GeV before being injected to the Super Proton Synchrotron (SPS). The SPS raises their energy to 450 GeV. Finally, the beams are injected to the main LHC rings and circulate in opposite directions until reaching the nominal energy. The beams collide at 4 interaction points where the ALICE (An LHC Heavy Ion Experiment), ATLAS (A Toroidal LHC Apparatus), CMS, and LHCb (LHC beauty experiment) experiments are located. Figure 2.1 (right) shows the basic layout of the LHC main ring which has eight arcs and eight straight sections. The experiments are located at the straight sections. ATLAS and CMS are the two general-purpose experiments located at Point 1 and Point 5, respectively.

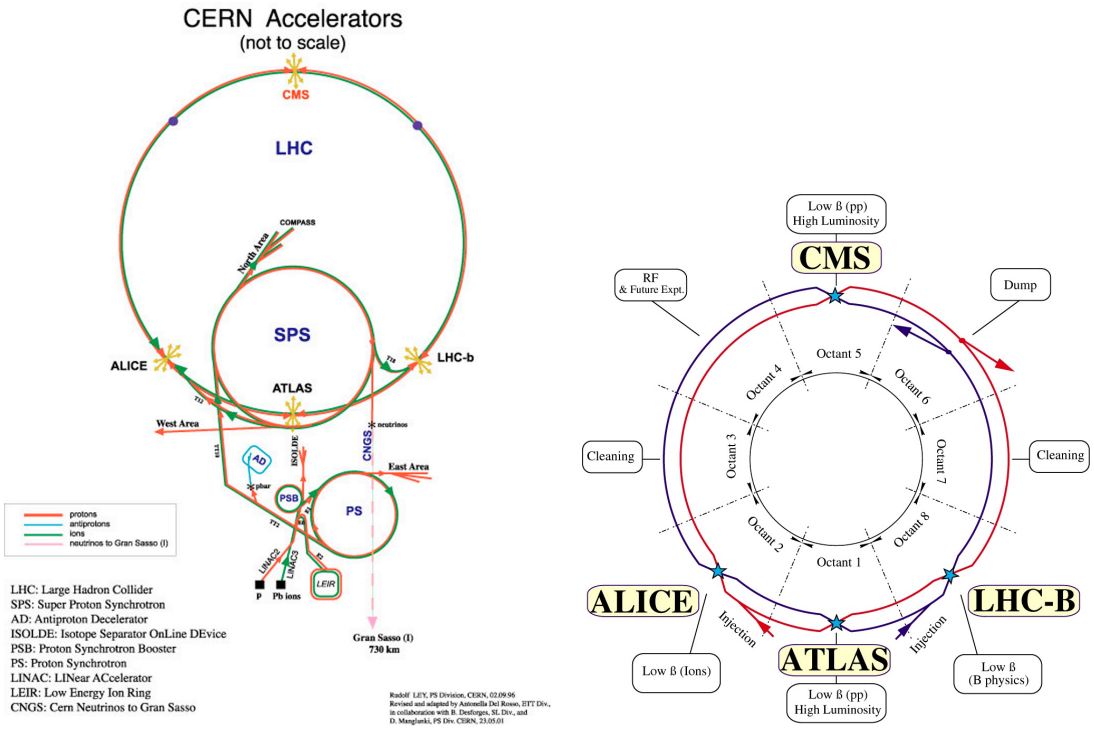

Figure 2.1: The LHC accelerator complex (left) and the main ring layout (right)

At design, the beams are packed in a large number of closely spaced bunches

(3,564 in total along the LHC orbit) and separated in time by 25 ns (approximately 7.5 m). However, only 2835 bunches are used for collisions with the detailed structure decided by the injection scheme and the properties of the dump system. The beams cross each other at a small angle (200 μrad) at the interaction points in order to avoid unwanted parasitic collisions away from the center of the detector [3]. The luminosity is given by:

$$L = \frac{N^2 k_b f \gamma}{4\pi \epsilon_n \beta^*} F, \tag{2.1}$$

where N is the number of protons per bunch, k_b is the number of bunches, f is the revolution frequency, γ is the relativistic factor, ϵ_n is the normalized transverse emittance, β^* is the beta function value at the interaction point, and F is the reduction factor caused by the crossing angle ($\sim$0.9 at the LHC). Table 2.1 lists the nominal values of those parameters for the design instantaneous luminosity L = 10^{34} cm^{-2}s^{-1}.

N	k_b	f	ϵ_n	β^*
1.15×10^{11}	2835	400 MHz	3.75 μm.rad	0.5 m

Table 2.1: LHC beam design parameters[3]

.

The LHC NbTi superconducting magnets are designed to maintain an 8 T field. They are cooled by superfluid helium at a temperature below 2 K. The main part of the LHC rings contains 1232 two-in-one dipoles. As shown in Figure 2.2, two beams are kept in separated dipoles in the same cryostat. There are also quadrupole and multipole magnets to focus and stabilize the beams, respectively.

The first collisions at the LHC took place in November 2009 with an energy of 450 GeV per beam. The energy increased to 1.18 TeV per beam in December 2009 and later to 3.5 TeV in March 2010 which was maintained during 2010 run. The

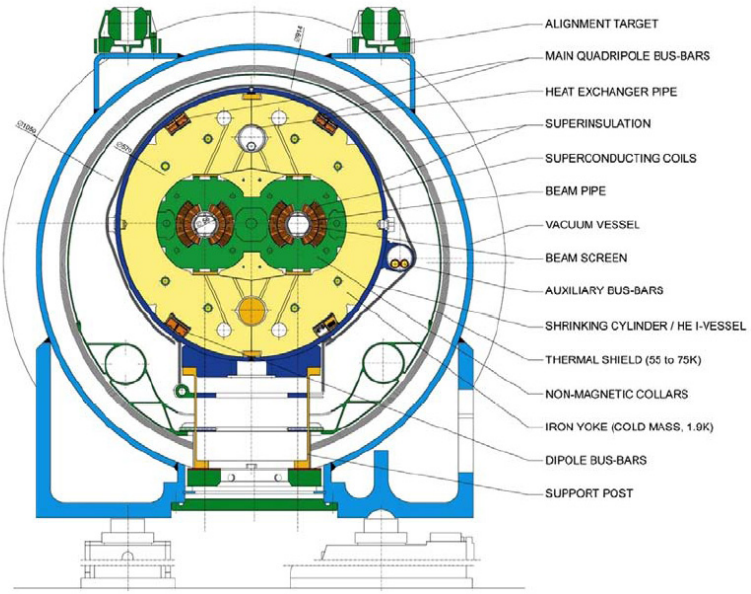

Figure 2.2: Cross section of an LHC diplole [8].

LHC will continue running at this energy in 2011. The instantaneous luminosity increased from 10^{27} cm^{-2}s^{-1} in March 2010 to its peak, 2×10^{32} cm^{-2}s^{-1} in October 2010. Figure 2.3 shows the integrated luminosity evolution of LHC in 2010. The integrated luminosity increased steeply toward the end of the run, and the LHC delivered a total of 47 pb^{-1} of collision data in 2010.

2.2 The CMS Detector

2.2.1 Overview

CMS uses a right-handed coordinate system, where the x-axis points radially inward toward the center of the LHC, the y-axis points vertically upward, and the z-axis points along the counterclockwise beam direction (toward the Jura mountains from the LHC Point 5). We measure the polar angle θ with respect to the z-axis and define

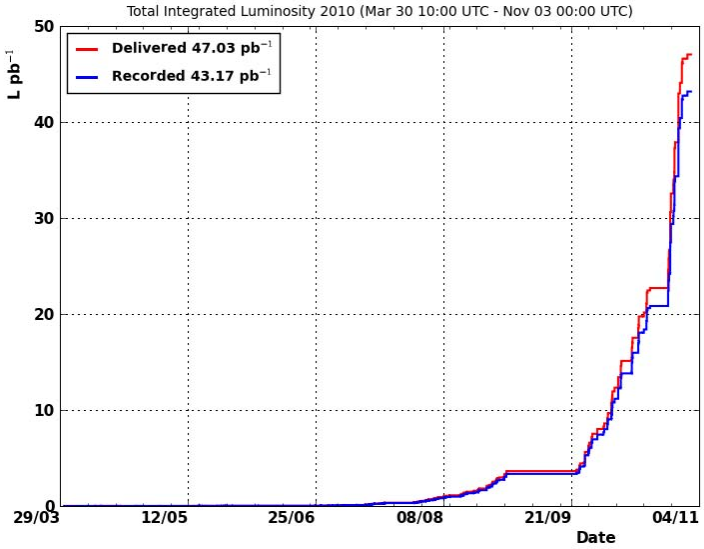

Figure 2.3: The integrated luminosity evolution in 2010 at CMS.

the pseudorapidity $\eta \equiv -\ln\tan(\theta/2)$. The azimuthal angle, ϕ, is measured with respect to the x-axis. The transverse quantities, for example transverse momentum or energy, are measured in the plane transverse to the beam direction. Thus, they are calculated from the x and y components.

The CMS detector is a multi-purpose detector designed to perform a wide range of high-energy collider physics at the LHC [44]. It is 21.6 m long, 14.6 m in diameter, and the total weight of 12,500 tons. It is located in the collision hall about 100 m underground at Point 5. Despite its huge size, the design of the CMS detector is compact compared to the ATLAS detector, with all subdetectors closely installed about a large-bore superconducting solenoid. The superconducting solenoid operates at 3.8 Tesla providing large bending power ($\sim$ 12 Tm). It is 13m long, and 6 m in diameter, which is large enough to contain the tracker and calorimeter systems.

The innermost subdetector is the all-silicon pixel detector whose purpose is to identify hits for track reconstruction. The 10-layer silicon microstrip detector, which

has a cylindrical shape of 5.8 m length and 2.6 m diameter, is placed between the pixel detector and the electromagnetic calorimeter. The electromagnetic calorimeter (ECAL) covers up to $|\eta| \leq 3$ and is made of lead-tungstate scintillating crystals with a thickness of 25 radiation lengths. The CMS hadronic calorimeter (HCAL) is placed after the ECAL with coverage up to $|\eta| \leq 5$. Finally, there are 4 muon stations installed outside the solenoid in the steel return yoke.This ensures robust muon track reconstruction and geometric coverage up to $|\eta| < 3$.

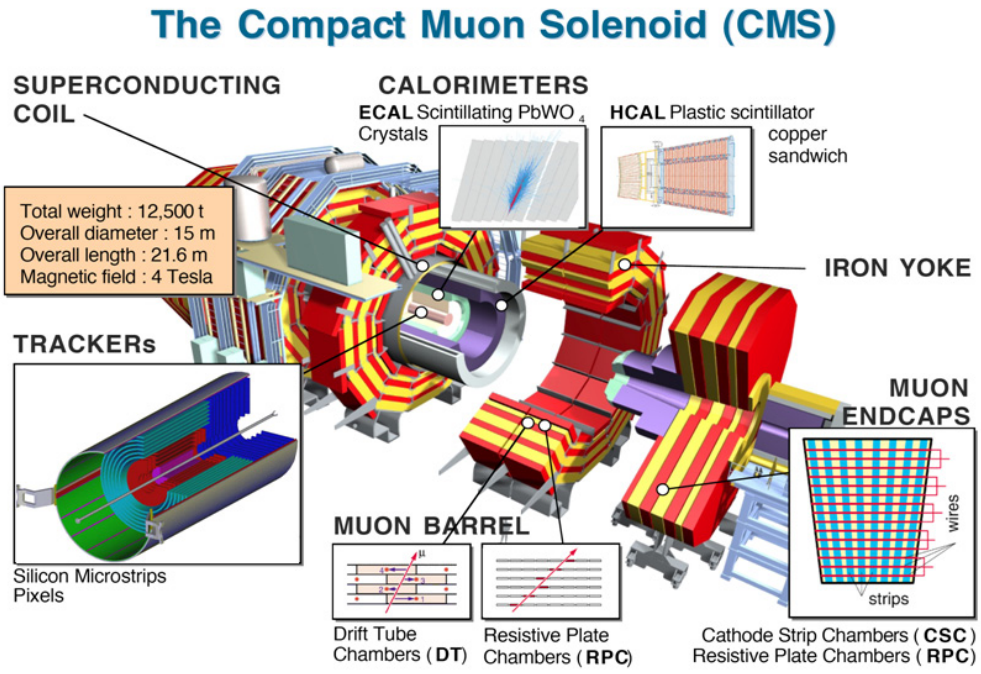

Figure 2.4: An overview of the CMS detector.

2.2.2 The Tracker

The LHC produces about 1000 particles traversing the tracker for every bunch crossing ($\sim$ 25 ns interval) at peak luminosity [44]. This requires a high-granularity and fast-response tracker to reliably reconstruct particle trajectories and vertices. Be-

cause of this, the CMS tracker is constructed entirely with silicon technology. The total active silicon area of CMS tracker is 200 m^2 and is composed of 1440 pixel and 15148 strip modules [44]. Figure 2.5 shows the layout of the CMS tracker. The maximum coverage of the tracker is $|\eta| \leq 2.5$. The pixel detector has 3 layers in the

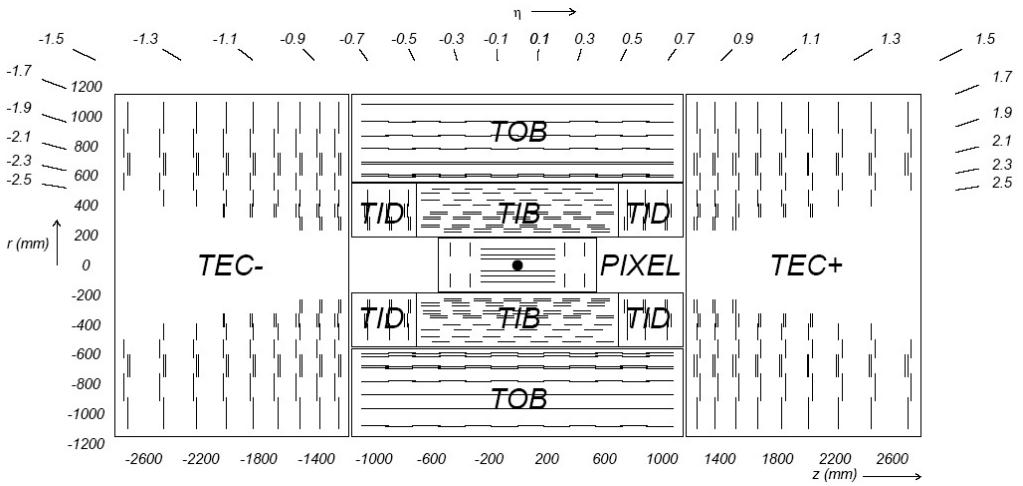

Figure 2.5: The tracker geometry.

barrel located between 4.4, 7.3 and 10.3 cm from the center of the detector. Each detector is 53 cm long. At the endcap, it is enclosed by 2 hollow disks with a radius of 6 and 15 cm. The inner and outer disks are at $|z|$=34.5 cm and $|z|$ =46.5 cm, respectively. There are about 66 million hybrid pixel cells in an approximately 100×150 μm square shape. Because of the high density of those small elements, the spatial resolution is approximate 10 μm in the r$-\phi$ plane and 20 μm in the z direction.

The pixel detector is surrounded by the silicon-strip detector. In the barrel, it includes the Tracker Inner Barrel (TIB) and the Tracker Outer Barrel (TOB). The TIB has 4 layers with a half length of 65 cm, and the TOB has 10 layers covering 110 cm in z at each side ($|z| < 220$ cm). The endcap region is covered by the Tracker End Cap (TEC) and the Tracker Inner Disks (TID). The 3-disk TID are embedded between the TIB and TEC. Each TEC is composed of 9 disks and extends the

longitudinal coverage from $|z|$=120 cm to $|z|$ =280 cm.

The silicon-strip detector is built from 15148 modules of 24244 sensors with 9.3 million strips. Depending on where the module is mounted, the strip pitch ranges from 80 to 180 μm. Some of the layers and rings (layers 1 and 2 for TIB and TOB; rings 1 and 2 for TID; rings 1, 2 and 5 for TECs) use a double-sided configuration in which two microstrip detector modules are mounted back-to-back with a stereo angle of 100 mrad. The purpose is to measure a second coordinate (z in the barrel and r on the disks). The geometry arrangement of the tracker provides at least nine hits in the strip detector with $|\eta| < 2.4$. Among these hits, at least four are two-dimensional measurements with a resolution of 230 and 530 μm in the TIB and TOB, respectively.

Figure 2.6 shows the expected resolutions of transverse momentum and reconstruction efficiency as a function of pseudorapidity for single muons with transverse momenta of 1, 10 and 100 GeV. The transverse resolution is less than 2% in the barrel and increases in the endcap. The reconstruction efficiency can be as good as 99% for muon in much of the acceptance range.

2.2.3 The Electromagnetic Calorimeter

The CMS electromagnetic calorimeter (ECAL) is a homogeneous scintillator calorimeter. It is built from 61,200 crystals in the barrel and 7324 crystals in each of the two endcaps [44]. Crystals are made of fast and radiation-hard lead-tungstate ($PbWO_4$). In order to improve the position resolution of electrons and photons, a preshower detector is placed in front of the endcap crystals. Scintillator light is produced by $PbWO_4$ crystals and converted to electrical pulses by avalanche photodiodes (APDs)

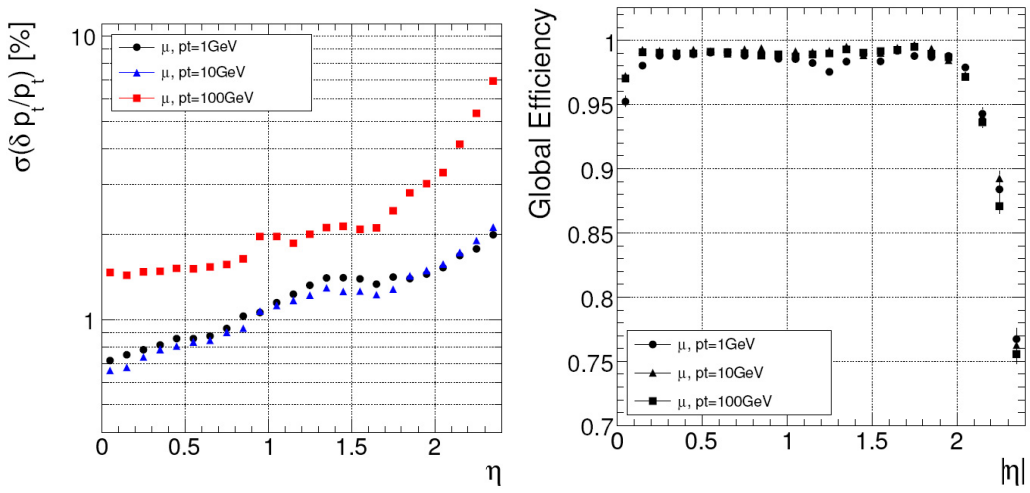

Figure 2.6: The tracker transverse momentum resolution (left) and the muon reconstruction efficiency (right).

in the barrel and vacuum phototriodes (VPTs) in the endcaps. The homogeneous ECAL calorimeters provides high granularity and excellent energy resolution, which makes detection of two photons from the postulated Higgs boson decay and for this search possible.

ECAL Layout and Mechanics

As shown in Figure 2.7, the CMS ECAL comprises 3 parts: the ECAL barrel (EB) covering $|\eta| < 1.479$, the ECAL endcaps (EE) extending from $1.497 < |\eta| < 3.0$, and the preshower detector placed in front of the ECAL endcaps. The EB is segmented by 360 folds in ϕ and 2×85 folds in η. The crystal front face centers are at a radius of 1.29 m. In order to avoid cracks aligned with particle trajectories, the crystal axes make a small angle (3^0) with respect to the vector from a nominal interaction vertex, in both ϕ and η projections. In the EB, the crystals of each half-barrel are grouped in 18 supermodules (spanning 20^0 in ϕ). Each supermodule comprises four modules. The first module has 500 crystals and each of the 3 remaining modules

contains 400 crystals. Inside a module, crystals are grouped in submodules of 2×5 crystals to simplify the construction and assembly. The EE detector is identical in both sides. Each side is divided into 2 halves in a "D" ("Dee") shape. Each Dee has 3662 crystals organized in groups of 5×5 crystals called the supercrystal. Therefore, each Dee consists of 138 standard supercrystals and 18 special partial superclusters on the inner and outer circumferences.

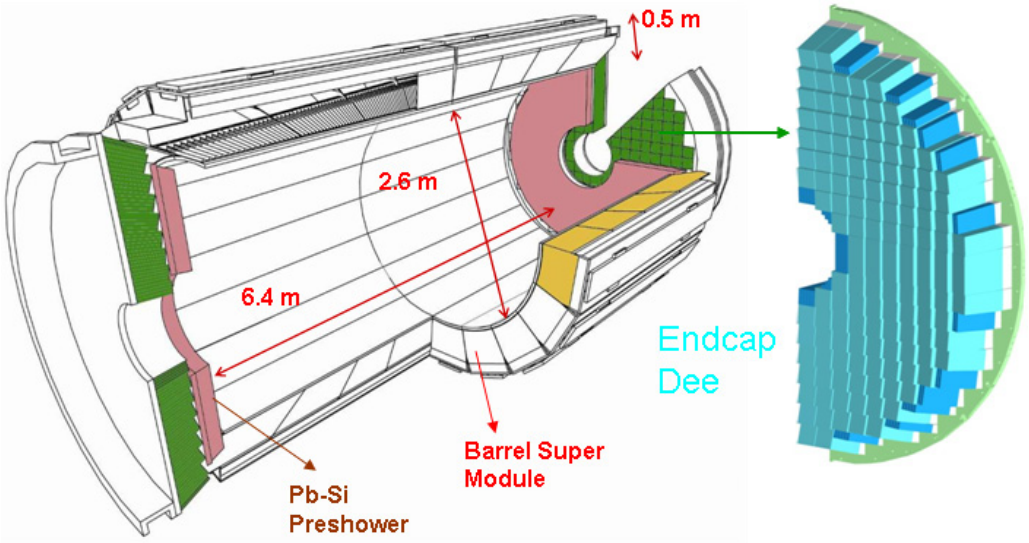

Figure 2.7: The ECAL layout.

Lead–tungstate Crystals

The $PbWO_4$ crystal is an appropriate choice for building a fine granularity and a compact calorimeter. It has a high density (8.28 g/cm^3), a short radiation length (0.89 cm), and a small Molière radius (2.2 cm). Its scintillation time is short. About 80% of the scintillation light is emitted in 25 ns, which is the LHC bunch crossing interval. However, the light output is relatively low and varies with temperature change (-2.1%^{0}C^{-1} at 18^{0}C). The scintillation emission spectrum has a broad maximum at 420-430 μm, which matches the wavelength range of good quantum efficiency of APDs and VPTs. In the barrel, the crystal front face cross-section is 22×22 mm^2

or approximately 0.0174×0.0174 in $\eta - \phi$ space. This size is approximately the Molière radius in lead tungstate. The crystal length is 230 mm corresponding to 25.8 radiation lengths (X_0). Most of the crystal faces are polished except one lateral face in order to make the light collection uniform. In the endcap, the crystals have a rear face cross section of 30×30 mm^2, a front-face cross section of 28.62×28.62 mm^2 and a length of 220 mm (24.7 X_0). Figure 2.8 shows a barrel and a endcap crystal and attached photodetectors.

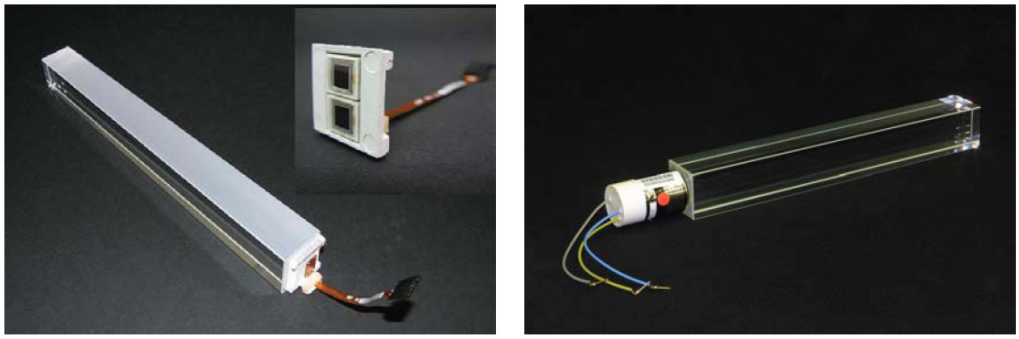

Figure 2.8: ECAL crystals in EB (left) and EE (right). The photodetectors are attached to the crystals at the rear surfaces.

The ECAL Photodetectors

The photodetectors are attached to the end of scintillating crystals and convert scintillation light to electronic pulses. The requirements for a photodetector are fast, radiation tolerant, and able to operate in the longitudinal 4 T field. The choices of photodetector technologies, avalanche photodiode (APD) for the barrel and vacuum phototriodes (VPT) for the endcap, are driven by the configuration of the magnetic field and the expected level of radiation. VPTs have lower quantum efficiency and internal gain compared to the APDs. However, this drawback is compensated for by their larger surface coverage on the back face of the crystals. A pair of APDs is attached to a crystal and each APD has an active area of 5×5 mm^2. Each VPT has

a diameter of 25 mm and an active area of approximately 280 mm^2. One VPT is glued to the back of each crystal.

Preshower Detector

The main purpose of the preshower is to provide $\pi_0 - \gamma$ separation. At high rapidity, two photons from π_0 decays are close together and not resolved in ECAL crystals. Therefore, $\pi_0 s$ are recognized as fake photons and contribute to the backgrounds in an analysis with photons. A high-granularity silicon preshower detector resolves these two photons; thus the backgrounds from π_0 are reduced. In the Higgs search in diphoton channel, about half of the Higgs decays results in one photon in the ECAL endcap, so the non-prompt photon reduction in the ECAL endcap is necessary to suppress the overall background.

The preshower detector is a sampling calorimeter, which is located in front of the endcap ECAL and covers a fiducial region $1.653 < |\eta| < 2.6$. It consists of two lead layers to initiate electromagnetic showers from incoming photons or electrons. A silicon-strip plane with a pitch of 2 mm is placed right after each lead radiator to measure the deposited energy and the transverse shower profiles. The orientations of the strips in the two planes are orthogonal. Figure 2.9 shows the layout of preshower sections. The total material thicknesses before the first and the second silicon sensor plane are 2 X_0 and 1 X_0, respectively. Therefore, about 95% of single incident photons start showering before reaching the second sensor plane. The energy deposited in 2 mm pitch silicon strips is used to determine the impact position of electromagnetic showers using a charge-weighted-average algorithm. The accuracy is very good, $\sim$300 μm at 50 GeV. This energy measurement is also used in the correction of energy measured by crystals, which preserves the excellent energy resolution of the

ECAL.

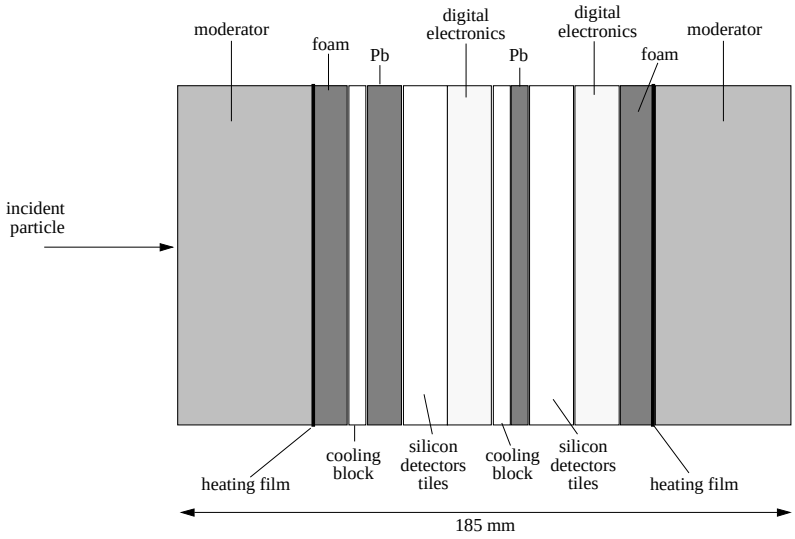

Figure 2.9: Arrangement of the preshower layers.

Energy Resolution

The ECAL energy resolution is parametrized as:

$$(\frac{\sigma}{E})^2 = (\frac{S}{\sqrt{E}})^2 + (\frac{N}{E})^2 + C^2 \tag{2.2}$$

where S is the stochastic term, N is the noise term, and C is the constant term. This parametrization is valid if the shower leakage from the rear of the calorimeter is less important (energy is below about 500 GeV). The contribution to S comes from fluctuations in the lateral shower containment, photostatistics and energy deposition in the preshower absorber (if present). The electronic, digitization and pileup noises contribute to the noise term. The constant term is caused by non-uniformity of the longitudinal light collection, intercalibration errors and leakage of energy from the back of the crystal.

The ECAL energy resolution is measured in the 2004 test beam for electron beam with momentum between 20 and 250 GeV/c. The result is showed in Figure 2.10, in which the stochastic, noise, constant terms are 2.8%, 0.12% and 0.3%, respectively. For an unconverted photon with shower energy $\sim$ 100 GeV, the constant term dom-

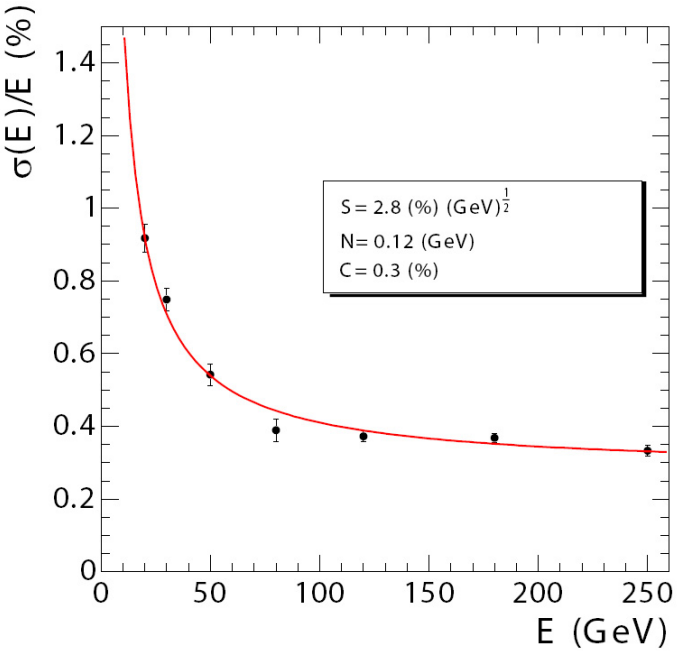

Figure 2.10: ECAL energy resolution.

inates. Therefore, the ECAL energy resolution depends strongly on the quality of the calibration. The particle energy in the ECAL is estimated by [45]:

$$E = F \times \sum_{clustercrystal} G(GeV/ADC) \times C_i \times A_i, \tag{2.3}$$

where F is the additional energy correction factor, which depends on particle type, energy and pseudorapidity. For electron, this factor takes into account for the shower leakage and the bremsstrahlung losses; G is the ECAL energy scale for ADC to GeV conversion; A_i are the reconstructed amplitudes in ADC counts; and C_i are the inter-calibration constants, which come from channel-to-channel variation. Details at the method to estimate C_i and G using the collision data are discussed in reference [45].

2.2.4 The Hadronic Calorimeter

The CMS hadronic calorimeter (HCAL) is a sampling calorimeter made of layers of dense absorber material and active material. The absorber material is brass or steel and the active material is scintillator. The hadronic calorimeter is vital for jets and missing transverse energy measurements. It includes four subsystems: the Hadronic Barrel (HB), the Hadronic Endcap (HE), the Hadronic Outer (HO) and the Hadronic Forward (HF) calorimeters.

The HB covers region $|\eta| < 1.3$ and is placed in the gap between the ECAL outer extent (R = 1.77 m) and the magnet coil inner extent (R = 2.95 m). Its thickness is limited to 5.8 hadronic interaction lengths at $\eta = 0$ and increases to 10 interaction lengths at $|\eta| = 1.2$ [44]. Therefore, the HO, which is placed outside the solenoid and covers $|\eta|$ <1.26, is intended to catch the energy leakage from HB. The HE covers region $1.3 < |\eta| < 3.0$ and the HF, placed outside the magnet at z = $\pm$11.2 (from the interaction point to their front faces), covers the forward region $3 < |\eta| < 5.2$.

The HF calorimeter uses Cherenkov-based, radiation-hard technology consisting of quartz fibers and steel. The fibers are parallel to the beam direction. A half of the total number of fibers is long fiber which extend the full length of the HF detector (165 cm). Other half of the total number of fibers is short fiber which stops at a distance of 22 cm from the front face of the HF. The purpose of this arrangement is to distinguish the electromagnetic and hadronic showers, since a electromagnetic shower starts to develop earlier than the hadronic shower and deposits most of its energy in the long fibers while a hadronic shower starts late and deposits most of its energy in the short fiber.

The HB and HO are segmented in towers of 0.087×0.087 in $\eta - \phi$ space. The

HE has the same granularity up to $|\eta| = 1.74$, after that the η segmentation varies from 0.09 to 0.35 and the ϕ segmentation is 0.175. In the HF, the segmentation is 0.175×0.175 and 0.175×0.35 at $|\eta| < 4.7$ and $|\eta| > 4.7$, respectively [9]. Figure 2.11 shows the segmentation of the HCAL.

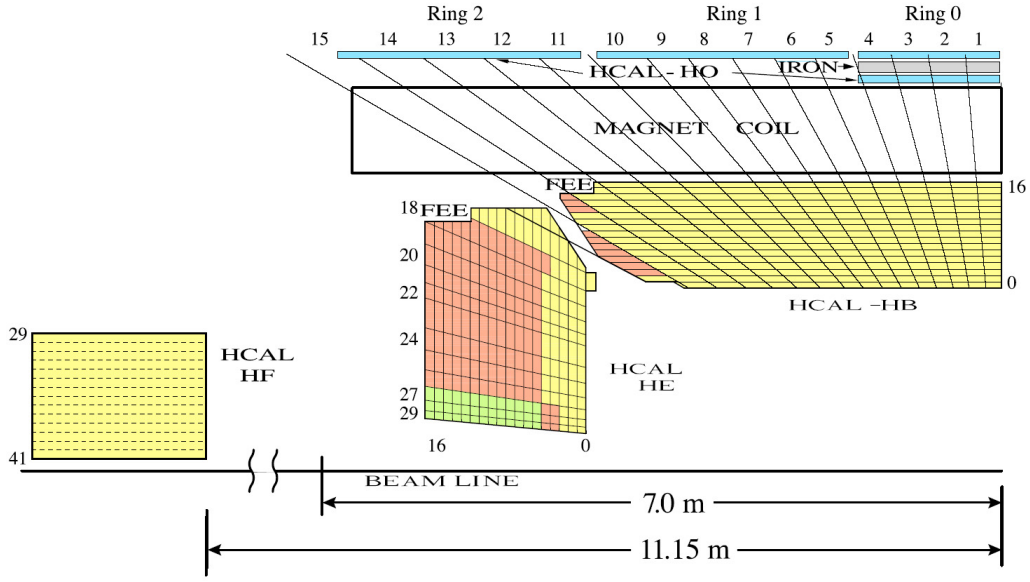

Figure 2.11: The schematic view of the CMS hadronic detector [9].

Light from the scintillation tiles is carried out by the embedded wavelength-shifting fibers. There are 17 scintillation layers in each HB and HE tower. The light of all scintillation layers are optically added in the HB. In the HE, the towers are divided in depths and the light from scintillation layers at the same depth are added. Finally, light signals are read by hybrid photodetectors (HPD). In the HF, lights from the fibers are collected by photomultipliers (PMT) housed in the read-out boxes.

2.2.5 The Muon Detector

The CMS muon detectors are gaseous detectors used for muon trigger identification, charge and momentum measurements. They are composed of 1400 chambers of 3 types: 250 drift tube chambers (DT) in the barrel ($|\eta|$ <1.2), 468 cathode strip chambers (CSC) in the endcap disks (1.2< $|\eta|$ <2.4) and 610 resistive plate chambers (RPC). The RPCs are mounted together with both the DT and CSC. The DT technology is the choice for the barrel because of small neutron-induced background, low muon rate and uniform magnetic field (mostly contained in the return yoke) in this region. In the endcap, the muon rates and background levels are high and the magnetic field is large and non-uniform. Thus, cathode strip chambers (CSC) are used.

The DT chambers are installed in hollows of the 5-wheel return yokes and organized in 4 stations. In the first three stations, each DT chamber composes 12 layers of drift tubes arranged in 3 groups of 4. Two of these groups have wires along z used to measure the ϕ coordinate and the other group measures the z coordinate. There are no z measuring layers in the outermost DT station.

The CSC system is arranged in 4 stations perpendicular to the beam pipe and mounted on the endcap disks. Each CSC chamber is built from 6 cathode planes and anode wires. In order to measure the position of a muon hit, cathode planes are segmented into narrow trapezoidal strips projecting radially from the beam line and anode wires are aligned perpendicularly to the strips.

The RPCs are fast gaseous detectors, which are added to both barrel and endcap (up to $|\eta|$ <1.6). Their purpose is to provide fast, independent, and highly-segmented trigger and help to resolve ambiguities when there are multiple hits in a chamber.

In the barrel, 6 layers of RPCs are embedded, 2 in each of the first 2 stations, and 1 in each of the last 2 stations. In the endcap region, there is a plane of RPCs in each of the first 3 stations. This arrangement allows the trigger to use the coincidences between stations for reducing backgrounds, improving the time resolution of bunch crossing identification, and for achieving a good p_T resolution.

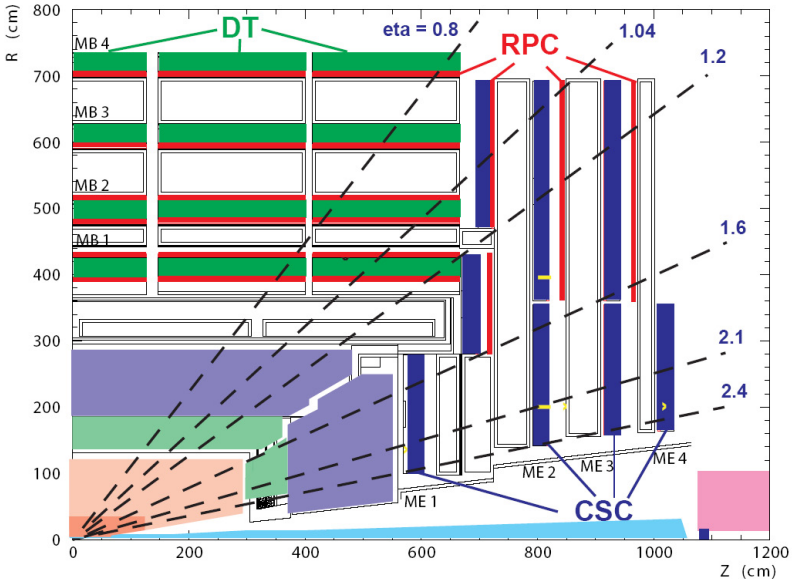

Figure 2.12: The muon detector layout [10].

2.2.6 The CMS Trigger

At the design instantaneous luminosity, 10^{34} cm^{-2}s^{-1}, the LHC crossing rate is 40 MHz with about 20 simultaneous pp collisions in each crossing. Because of this enormous rate, it is impossible to store all the events, and a trigger system is used to reduce dramatically the rate (by a factor 10^6) by selecting just the most interesting events for physics analyses. The CMS trigger has a 2-level architecture. The Level-1 trigger (L1) is built from fast custom hardware processors with the maximum bandwidth of 100 kHz (the practical maximum output rate is 30 kHz, assuming an approximate safety factor of three). The L1 trigger system is divided in 3 subsystems:

the L1 calorimeter trigger, the L1 muon trigger, and the L1 global trigger. The muon trigger system comprises 3 subsystems corresponding to 3 muon subdetectors, the Drift Tube Trigger in the barrel, the Cathode Strip Chamber (CSC) trigger in the endcap and the Resistive Plate Chamber (RPC) covering both barrel and endcap.

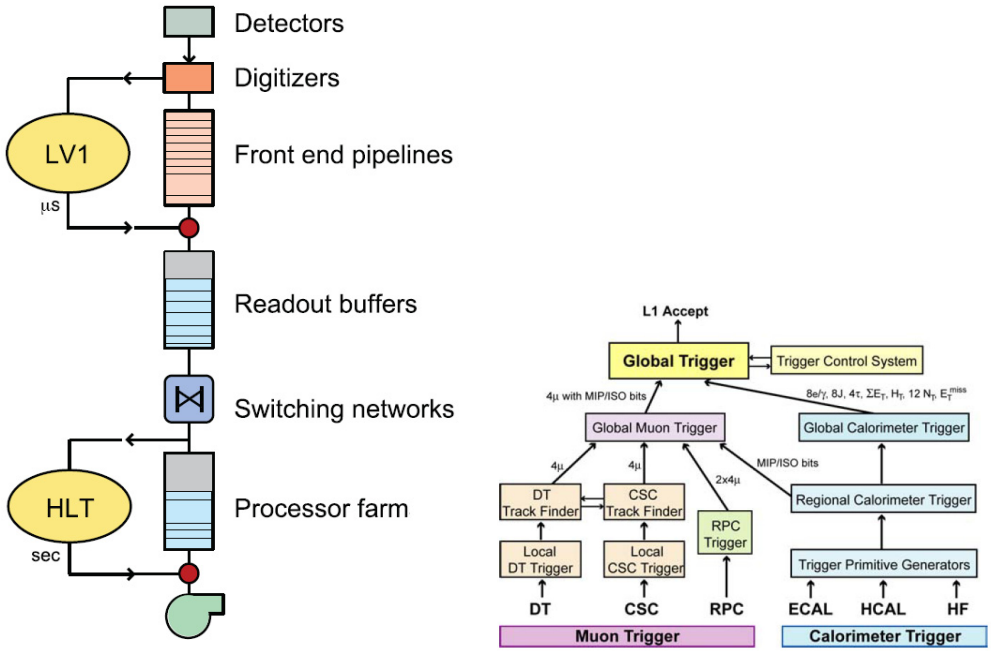

Figure 2.13: The structure of the CMS trigger (left) and the L1 trigger (right) [10].

Trigger information from the DT, CSC and RPC trigger systems is combined at the L1 global muon trigger and sent to the L1 global trigger. Up to four candidates from each of the DT and CSC triggers and up to eight candidates (four in the barrel, and four in the endcap) from the RPC trigger are sent to the L1 global muon trigger which in turn sends the four highest quality muons to the L1 global trigger. In the calorimeter trigger, the trigger primitives constructed from the energy sums in the trigger towers of the ECAL, HCAL and HF are generated by the Trigger Primitive Generator (TPG). The TPG information is transmitted to the Regional Calorimeter Trigger (RCT), which combine them together into regions of the size of 4 x 4 towers in the central region and somewhat larger size in the forward direction. These regions are transferred to the Global Calorimeter Trigger (GCT). The GCT

finds isolated or non-isolated electron/photon, tau, and jet candidates and the sum of transverse energy. It performs a candidate sorting based on their ranks and forwards the top four of each type to the global trigger. The total transverse energy and total missing energy vector are also calculate by the GCT. Finally, the GCT information is forwarded to the global trigger, which issues the trigger decision. This trigger decision is transmitted to all of the subdetector front-end and readout systems by the Trigger Timing and Control system. The L1 pipeline data storage time is 3.2 μs. Therefore, the L1 trigger calculations is limited in many cases in less than 1 μs [46].

The High-Level Trigger (HLT) is a software system implemented in a filter farm of commercial processors which reduces further the event rate from L1 trigger to the order of 100 Hz before data storage. The HLT access to complete read-out data is via a 100 Gb/s switching network. Thus, it has the capacity to perform sophisticated calculations based on reconstruction algorithms similar to those of the off-line analysis.

Chapter 3

Event Reconstruction

The purpose of this chapter is to review the reconstruction of objects from signals in subdetectors. These signals are produced when particles from the interaction points transverse through detector materials. Trajectories of charge particles are measured in the tracker (Section 3.1). Measurements of muon tracks use information from both the tracker and the muon chambers (Section 3.3). Electrons and photons are measured in the electromagnetic calorimeter (ECAL) (Section 3.5). The electron tracks are reconstructed in the tracker. Finally, jets and missing transverse energy are reconstructed from the energy deposits in the calorimeter towers (Section 3.4). A calorimeter tower is a combination of a hadronic (HCAL) tower and electromagnetic crystals located in front of this HCAL tower.

3.1 Track Reconstruction

Tracks are reconstructed by the Combinatorial Track Finder (CFT) following these steps: local reconstruction, seed generation, pattern recognition, final track fit and track selection. The track reconstruction in CMS begins with hits reconstructed by local reconstruction in the pixel and strip detector. The seed generation step defines initial trajectory parameters and their uncertainties. At least 3 hits or 2 hits and a beam constraint are required to identify the five parameters needed for trajectory building. Reconstructing track seeds from the innermost layer of the tracker is preferred more due to the higher density of the read-out channel per square unit. Furthermore, because of fewer material budget placed in front of the innermost layer compared to the outermost layer, the chance that a particle interacts with material before reaching a innermost layer is low. Thus, the hit position identification is more precise. These conditions ensure precision of the initial track parameter estimation. These are common seeding types used in CMS: pixel triplets, pixel and strip pairs with a vertex constraint or with a beam-spot constraint, and strip-only pairs with a beam-spot constraint [47].

The pattern recognition is based on the Kalman filter [48]. Beginning with a coarse estimation of track parameters from the track seeding, the filter proceeds from layer to layer to find compatible hits. If a hit is found, it is included in the trajectory and the track parameters are updated with information from this hit. The iteration stops when the outermost layer is reached or no compatible hit is found. This step results in a number of track candidates satisfying requirements on the normalized χ^2 and the number of valid and invalid hits. The final track fit refits the track candidates for a full track information.

The track selection step removes a large number of misidentified tracks. In the current CMS implementation, the CFT iterates six times [49]. After an iteration, the unambiguous track clusters assigned to tracks are removed from the cluster iteration used in the next iteration. The tracks which are likely misidentified are also rejected. The remaining tracks are assigned a quality flag based on a restriction on the normalized χ^2, the longitudinal and transverse impact parameters with respect to the beam-spot, and their significance. Poor-quality tracks are further rejected and a high-purity flag is assigned to tracks that pass the tightest selection [49]. Figure 3.1 shows the impact parameter resolution in 2010 pp collision data.

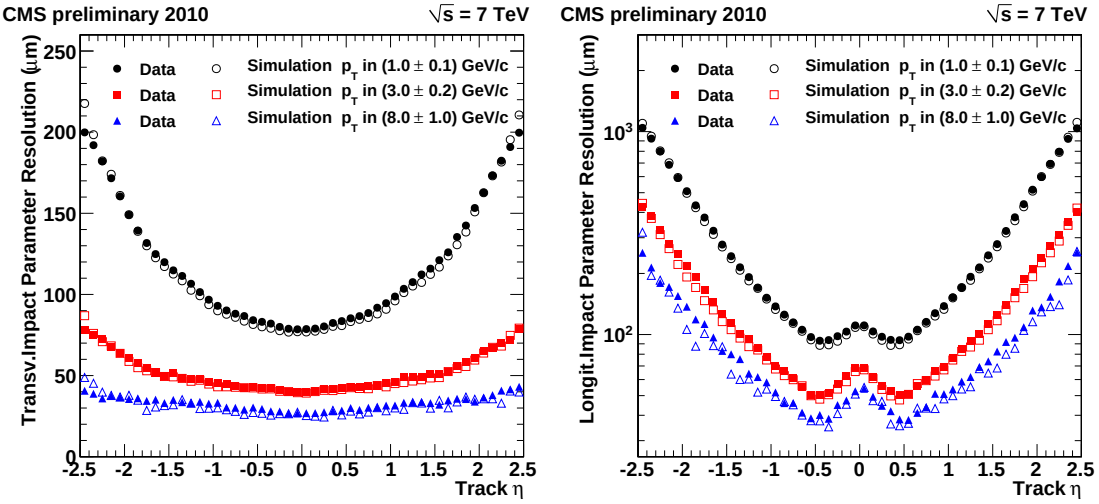

Figure 3.1: The track impact parameter resolutions. The results from collision data are compared to MC simulation. [11]

3.2 Vertex Reconstruction

The primary vertex reconstruction finds the location of the interaction vertex and its uncertainty. The reconstruction algorithm uses reconstructed tracks, which are close together when comparing their impact parameters. The tracks are required to

originate from the primary interaction region and satisfy criteria on the transverse impact parameter significance with respect to the beamspot, number of strip and pixel hits, and the normalized χ^2. The next step is to form vertex candidates by grouping tracks that are separated from their closet neighbor in z_0, the z coordinate of the impact point, by less than 1 cm.

An adaptive vertex fit is performed [50] on vertex candidates containing at least two tracks. The best estimates of vertex parameters (position and covariance matrix) are found together with parameters to indicate fit quality, for example χ^2/n_{dof} and the track weights. Track weights are from 0 to 1 and are based on the track compatibility with the common vertex. The reconstruction efficiency is approximately 100% for primary vertex containing more than 2 tracks with transverse momenta greater than 0.5 GeV. In the minimum bias data at 7 TeV, the x(y) and z resolution are close to 25 μm and 20 μm for primary vertex with more than 30 tracks [11].

3.3 Muon Reconstruction

Muon track reconstruction combines hits in the tracker and in the muon chambers. Muon tracks are reconstructed separately in the silicon tracker and muon chambers (standalone muon track). These are merged by outside-in (global muon reconstruction) or inside-out (tracker muon reconstruction) algorithms. In the global muon reconstruction, a standalone muon track is matched with a tracker track and the hits of those tracks are combined in a common fit to find the global muon track. This method improves the momentum resolutions of high p_T tracks ($p_T \geq$200 GeV) compared to tracker-only fit. In the tracker-muon approach, tracker tracks with $p_T >$0.5 GeV/c and p>2.5 GeV/c are considered as muon candidates and they are

extrapolated to the muon systems to find a matched muon segment found from DT or CSC hits. Energy loss and uncertainty due to multiple scattering are considered in the extrapolation. If the match is found, the tracker track is considered as tracker-muon track. Because the method requires only a matched single muon segment in muon chambers, it has higher reconstruction efficiency for low p_T tracks compared to the global muon reconstruction.

About 1% of muon from collisions fail to be reconstructed by the two methods described above but are found by the stand-alone tracker-only approach [12]. Finally, muon candidates found by all three algorithms are merged to a single collection. Each candidate contains available information from the stand-alone, the tracker-track and the global fit. If two candidates are found by Tracker Muon and Global Muon and share the same tracker track, they are merged into a single candidate. If a stand-alone muon track shares a muon segment with a tracker muon and is not included in a global muon track, it is merged to the tracker muon. Figure 3.2 shows the reconstruction efficiency of the global muon.

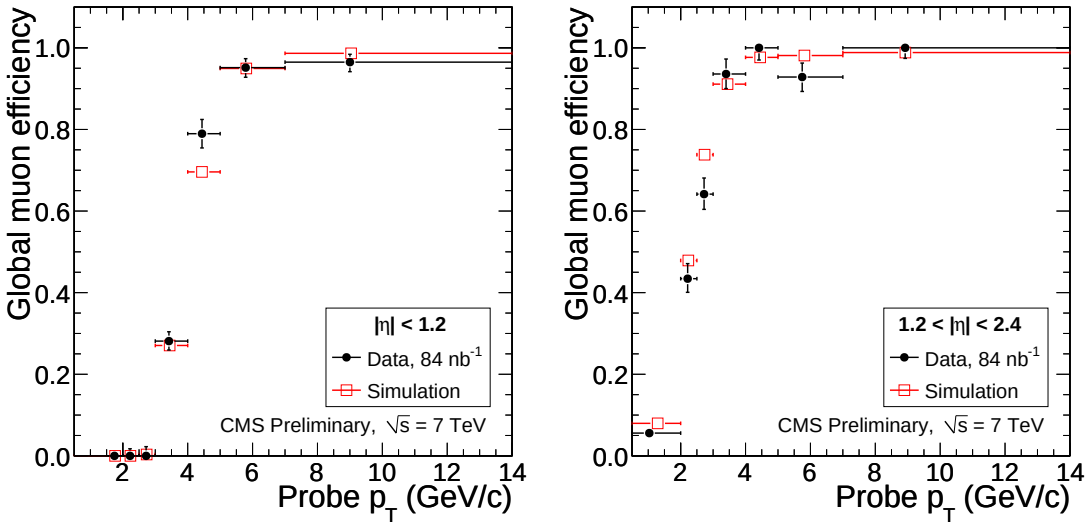

Figure 3.2: The muon reconstruction efficiency for Global Muons in data compared to simulation given that a tracker track exists. [12]

3.4 Jet and Missing Transverse Energy Reconstruction

The fragmentation of quarks and gluons in the final state results in a stream of collimated particles. A calorimeter algorithm clusters energy deposits in the calorimeter towers to form jets. A calorimeter tower is a combination of HCAL cells and ECAL crystals. One HCAL cell corresponds to 5×5 ECAL crystals in the barrel ($|\eta|$ <1.4). In the endcap, the HCAL-ECAL mapping is more complex. A successful algorithm should be collinear-safe and infrared-safe [51]. Collinear-safety requires that the outcome remains unchanged if the energy of a original single particle is distributed among two collinear particles. Infrared-safety means that the result of the jet finding is stable against the addition of soft particles. Below are some of the algorithms used in CMS:

- Iterative cone: this is a simple cone-based algorithm which performs iterative searches for stable cones. Starting from a seed crystal or particle, all inputs within $\sqrt{\delta\eta^2 + \delta\phi^2}$ ≤R are associated with a jet. R is the cone-size parameter (popular choice is 0.5). If the cone geometric center agrees with the (η, ϕ) location of the sum of the constituent four vectors, a jet is found. This algorithm is not collinear-safe and infared-safe but it is fast and has predictable calculation time. Thus, it is implemented in the HLT.

- Midpoint cone [52]: this method uses iterative cone technique to find stable cones. However, there are two improvements to address the infared-safe condition. Midpoints between each pair of (proto-)jets, which are closer than twice the cone radius R, are uses as additional seeds and each input can initially be associated with several protojets. A splitting and merging algorithm

is implemented to ensure that each input appears in one jet only. Despite these improvements, the algorithm is not infared-safe for pQCD order beyond NLO [52].

- k_T algorithm: the clustering is decided by distance quantities assigned for each protojet

$$d_i = (E_{T,i}^2)R^2 \tag{3.1}$$

$$d_{ij} = min(E_{T,i}^2, E_{T,j}^2 R_{ij}^2) \tag{3.2}$$

$$R_{ij}^2 = (\eta_i - \eta_j)^2 + (\phi_i - \phi_j)^2 \tag{3.3}$$

where $E_{T,i}$ is the transverse energy of i^{th} protojet, $R_{i,j}^2$ is the distance between two protojets. R^2 is a dimensionless parameter. The next step is to sort the list of d_i and d_{ij} and finds the smallest values. If the smallest value is d_i type, the corresponding protojet is considered as a jet and removed from the list. If the smallest value is d_{ij}, the protojet pair is recombined. The distances are recalculated and the whole procedure is repeated. The search stops when the list is empty. There is an extension to this method called anti-k$_T$ algorithm which uses these distance definitions [53].

$$d_{iB} = E_{T,i}^{2p} \tag{3.4}$$

$$d_{ij} = min(E_{T,i}^{2p}, k_{T,j}^{2p})\frac{R_{ij}^2}{R^2} \tag{3.5}$$

p is a parameter to tune the relative power of the energy and geometrical scales, R_{ij}. For p=1, this returns to the normal k_T algorithm and for p>0, the performance is similar to the k_T method. The anti-k_T jet-clustering algorithm corresponds to p=-1.

- SISCone (Seedless Infrared-Safe Cone) is a jet algorithm which is collinear-

and infrared-safe to all orders of pQCD. The calculation time is slightly higher compared to the Midpoint Cone algorithm [51].

There are four types of jets reconstructed in CMS. The differences between these are the combination of subdetector information to provide inputs for the jet clustering algorithm. The calorimeter jets are reconstructed from energy deposit in calorimeter towers by the clustering methods describe above. Utilizing the excellent momentum reconstruction of the tracker, calorimeter jets are combined with nearby charged tracks reconstructed in the tracker to form jet-plus-track jets [54]. The p_T response and the energy resolution of jets are improved due to better momentum measurements in the tracker. The particle flow algorithm is used to reconstruct PFlow jets [55]. A list of all particles reconstructed by all subdetectors is found and PFlow jets are reconstructed from this list. Finally, track jets are reconstructed based on well measured tracks in the central tracker [56].

Jet energy measured in the detector is corrected for a better measurement of particle jet energy. CMS adopts a factorized multi-step procedure for the jet energy correction: offset, relative and absolute corrections [57]. The offset correction removes the unwanted energy due to electronic noise and pile-up. The relative correction uniforms the jet response vs jet η with respect to a central control region chosen as a reference. Finally, the variation of jet response vs. p_T is removed by the absolute correction:

$$E_{corr} = (E_{uncorr} - E_{offset}) \times C_{Rel}(\eta, p_T^{''}) \times C_{Abs}(p_T^{'}) \tag{3.6}$$

where $p_T^{''}$ is the jet transverse momentum given by offset correction and $p_T^{'} = p_T^{''} \times C_{Rel}(\eta, p_T^{''})$ is the transverse momentum given by the offset and relative correction. At the initial stage of LHC running, the correction is done in MC simulation. It

can also be done using physics processes from the pp collision (dijet and photon+jet balance). Figure 3.3 shows the total jet-energy scale uncertainty in 2010 collision data at 7 TeV. The conservative jet energy scale uncertainty is 5% for calorimeter jets, jet-plus-track jets and PFlow jets.

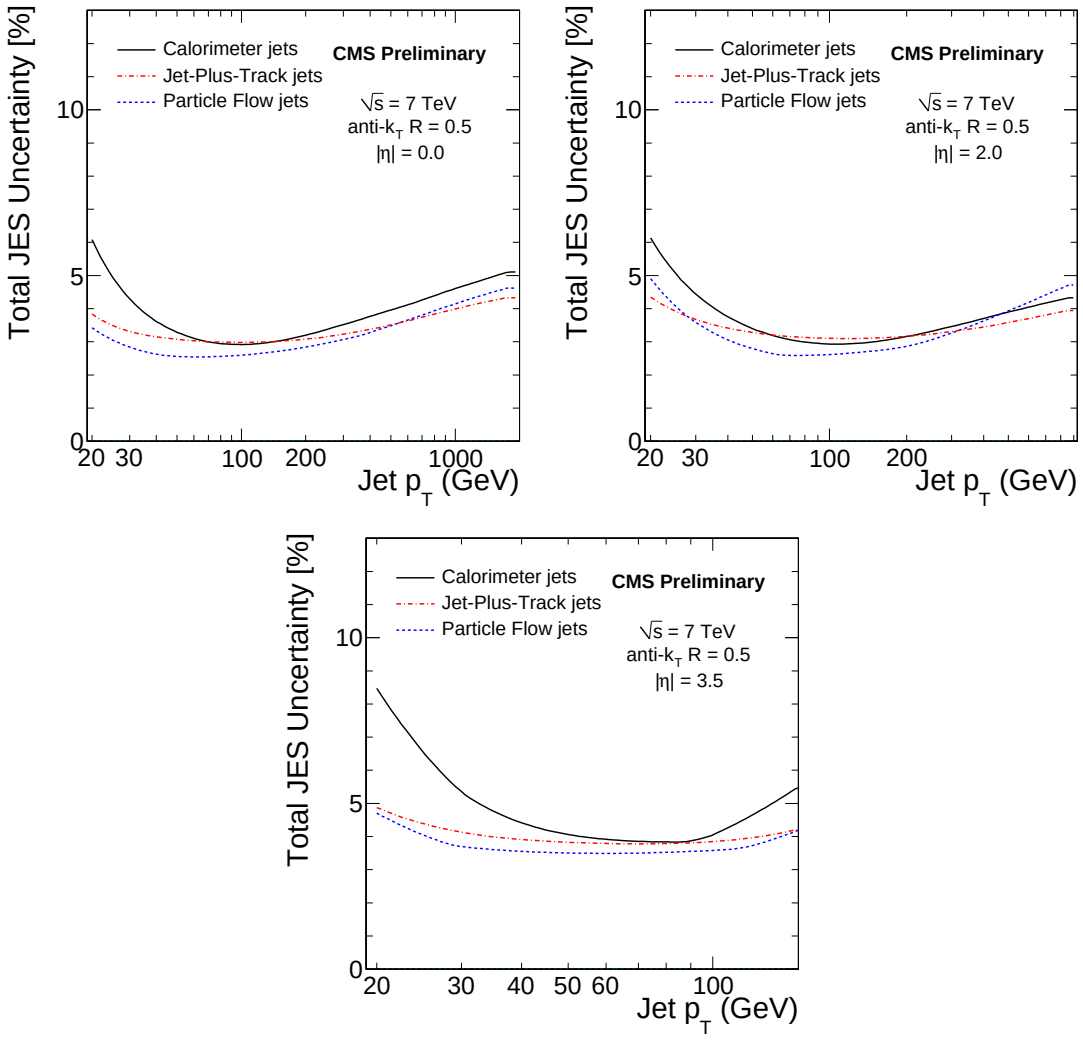

Figure 3.3: Total jet energy scale uncertainty as a function of jet p_T for different η values [13].

Weakly interaction particles such as neutrinos transverse the detector without depositing their energy. The missing transverse momentum is an indication of the production of such particles in the pp collision. The missing transverse energy is

defined as [58]:

$$\vec{\not{E}_T} = -\sum n(E_n \sin\theta_n \cos\phi_n \vec{i} + E_n \sin\theta_n \sin\phi_n \vec{j}) = \not{E}_x \vec{i} + \not{E}_y \vec{j}, \tag{3.7}$$

where n runs over all calorimeter input object, for example, energy deposit in towers or generated-level particle energy, $\vec{i}$, $\vec{j}$ are the unit vectors in the direction of the x and y axes. If there is no missing transverse energy from physics processes, the $\not{E}_x$ and $\not{E}_y$ distribute as Gaussians with zero mean and standard deviation σ, while the magnitude of missing transverse energy vector, $\not{E}_T$, distribution has the shape described by $\frac{2\pi}{\sigma}\theta(\not{E}_T) \times G(\not{E}_T, 0, \sigma)$. In this formula, $\theta(\not{E}_T)$ is the step function and G is the Gaussian function. The missing transverse energy resolution is estimated by the quadrature sum of the noise term A, stochastic term B and constant term C [58]:

$$\sigma(\not{E}_T) = A \oplus B\sqrt{\sum E_T - D} \oplus C(\sum E_T - D), \tag{3.8}$$

where $\sum E_T = \sum nE_n \sin\theta_n$ is the Scalar Transverse Energy and D is the offset caused by the noise effect and pile-up on $\sum E_T$.

CMS use four types of $\not{E}_T$: calorimeter-tower based (CaloMET), tcMET, calorimeter-jet based (MHT) and particle flow based (PFMET) $\not{E}_T$. The CaloMET and MHT are corrected in sequence for muons, jet energy scale effect, taus, underlying event/pile-up. Details are described in reference [58]. Instead of using jet energy scale correction, a track-base correction, which replaces the calorimeter tower response for charged particle momentum measured in the tracker, is applied for CaloMET [59]. This results in tcMET. The PF algorithm reconstructs individual particles with high precision. Thus, the PFMET is calculated from the charged and neutral particle energy deposit without the need of jet energy scale correction. Figure 3.4 shows the missing transverse energy of multijet events in 7 TeV collision data.

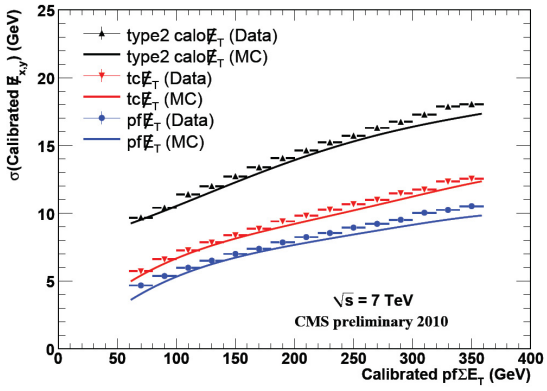

Figure 3.4: Calibrated $\not\!\!E_T$ resolution versus calibrated E_T sum from particle flow for different $\not\!\!E_T$ types. Shown are a comparison between data and simulation [14].

3.5 Photon and Electron Reconstruction

3.5.1 ECAL Clustering

The clustering methods used in CMS to reconstruct photon and electron objects are the hybrid and island algorithms [15].

The island algorithm forms clusters of crystals containing energy depositions from a shower around seed crystals. The energy of the seed crystals are above a certain threshold. The clusters are collected one-by-one while the search moves in η and ϕ directions. Figure 3.5 illustrates the algorithm. Starting from the seed crystal position, it moves in both ϕ directions and stops when there is an increase in energy or a hole (very low energy crystal). The search in the ϕ direction is repeated for each η step and in both η directions. The algorithm also stops in the η direction if it encounters an increase in energy or a hole. In order to cover the energy spread due to radiation, clusters are formed in a supercluster in a similar way as forming a cluster of crystals. Non-overlapping clusters around a seed cluster within narrow η window and much wider ϕ window are collected in a supercluster.

The hybrid algorithm clustering starts from a seed crystal which has maximum energy in the search region and $E_T > E_T^{hybseed}$, where $E_T^{hybseed}$ is about 1 GeV. Crystals are grouped in 1×3 or 1×5 dominoes aligned in η with the seed crystal. If the energy of the central crystal of the dominoes is more than E_{wing} (about 1 GeV), 1×5 dominoes are chosen. The domino grouping proceeds in N_{step} from the seed crystal in both directions (see Figure 3.5, right). The next step is to cluster these dominoes in ϕ requiring that a distinct cluster has a seed domino with $E > E_{seed}$ ($E_{seed} \sim 0.35$ GeV). Finally, a cluster of clusters is found analogous to the supercluster of island clusters.

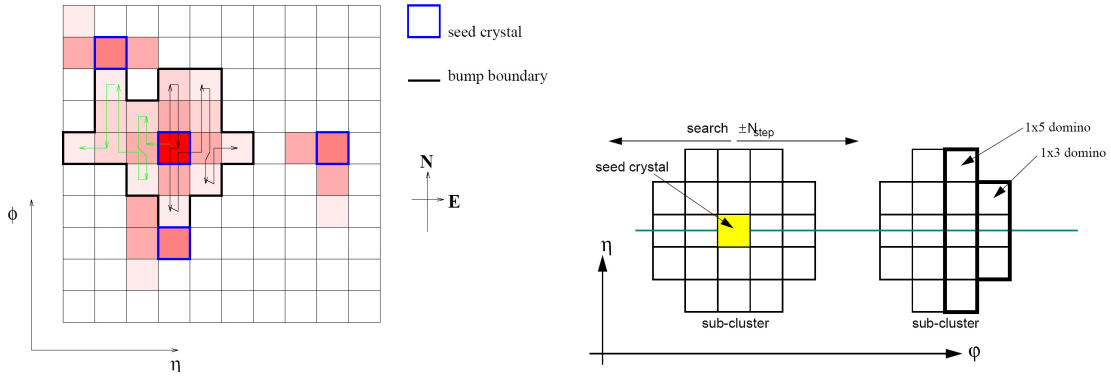

Figure 3.5: Island and hybrid clustering algorithm illustration [15]

3.5.2 Photon Candidate

The photon reconstruction starts from summing the photon shower energy deposits in the ECAL crystals. An array of 5×5 (3×3) crystals contains 97% (94%) the incident energy. Summing the energy measured in such fixed arrays gives the best performance for unconverted photons, or for electrons in the test beam [10]. However, the presence of the material in front of the ECAL causes the photon conversions and the energy deposit spread in ϕ due to the strong magnetic field (the strong magnetic field bends the electron and positron tracks, and they radiate in tracker material).

A supercluster that extends in ϕ is built to recover fully the photon energy. The superclusters are reconstructed by the hybrid algorithm, in the barrel, or the island algorithm, in the endcaps as described above. A small correction (1%) is applied to the supercluster energy in order to compensate for the lateral energy leakage due to the 3^0 off-pointing of the EB crystal and for the interaction with material in front of ECAL.

The R9 variable, defined as the ratio of energy contained in a 3×3 array of crystals (centred at the crystal with the highest deposited energy) to the supercluster energy, indicates the lateral spread of deposited energy. Figure 3.6 shows the R9 variable observed in data at 7 TeV. R9 approaches unity for unconverted photons or photons which convert very close to the ECAL. This quantity determines which method is used for the energy calculation. If R9 is above 0.94 (0.95) in the barrel (endcap), the photon energy is the energy of the 5×5 crystal array around the seed crystal (the highest energy crystal). Below this threshold, the energy of the supercluster is the photon energy. In the endcap, the energy deposit in the preshower detector is added to the energy of the ECAL clusters. The superclusters or 5×5 clusters are promoted to be the photon candidates if the HCAL activity around them is low.

3.5.3 Photon Identification

As described in the previous section, photon objects are reconstructed from corrected energy deposition of a supercluster or a 5×5 crystal array. A jet with a significant fraction of its energy concentrated in a neutral π^0 or η causes a large electromagnetic deposition in the ECAL. Therefore, a "fake" photon is reconstructed. In order to improve the photon purity, a set of identification requirements are applied to photon candidates. These identification requirements are mostly based on the isolation

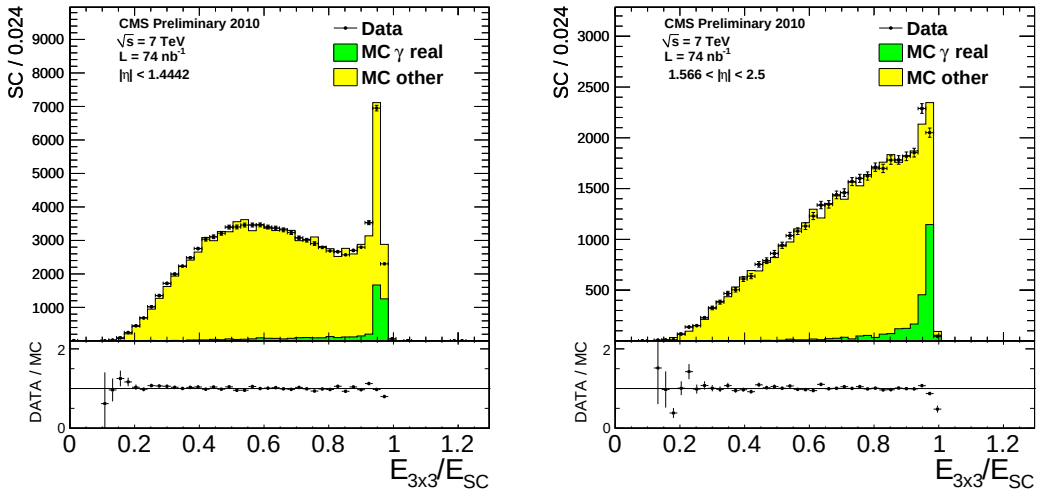

Figure 3.6: R9 distribution [16]

defined as:

- *HadronicOverEM* (HoverEM): The ratio between the hadronic energy and the photon electromagnetic energy within $\Delta R < 0.15$ of the photon. Here $\Delta R \equiv \sqrt{\Delta\eta^2 + \Delta\phi^2}$

- *Tracking Isolation* (TrkIso): The scalar sum of the transverse momentum of tracks ($\sum p_T$) associated with the primary event vertex surrounding the photon within a hollow cone of $0.04 < \Delta R < 0.40$ (a rectangular strip of $\Delta\eta \times \Delta\phi = 0.015 \times 0.400$ is excluded from the track p_T summation to allow for photons that convert into e^+e^- pairs).

- *ECAL Isolation* (EcalIso): The scalar sum of ECAL transverse energy ($\sum E_T$) surrounding the photon within $0.06 < \Delta R < 0.40$ (and excluding a $\Delta\eta \times \Delta\phi = 0.04 \times 0.400$ strip)

- *HCAL Isolation* (HcalIso): The scalar sum of HCAL transverse energy ($\sum E_T$) surrounding the photon within $0.15 < \Delta R < 0.40$.

The weighted width in η of the shower is used as an identification variable. We define the shower shape variable:

$$\sigma^2_{i\eta i\eta} = \frac{\sum_i^{5\times5} w_i(i\eta_i - i\eta_{seed})^2}{\sum_i^{5\times5} w_i}, w_i = max(0, 0.47 + \ln\frac{\mathrm{E_i}}{\mathrm{E_{5\times5}}}) \tag{3.9}$$

The distributions of the identification variables are shown in Figure 3.7, Figure 3.8, Figure 3.9, and Figure 3.10 for ECAL isolation, HCAL isolation, tracking isolation, and shower shape, respectively.

Although photons are not ionizing particles, they can converted into e^+e^- pairs in the detector through material interactions. Vetoing on a pixel seed, a hit found in the pixel layers associated with particle trajectory, suppresses electrons from being misidentified as photons while still allowing an appreciable acceptance for converted photons. This requirement is optional.

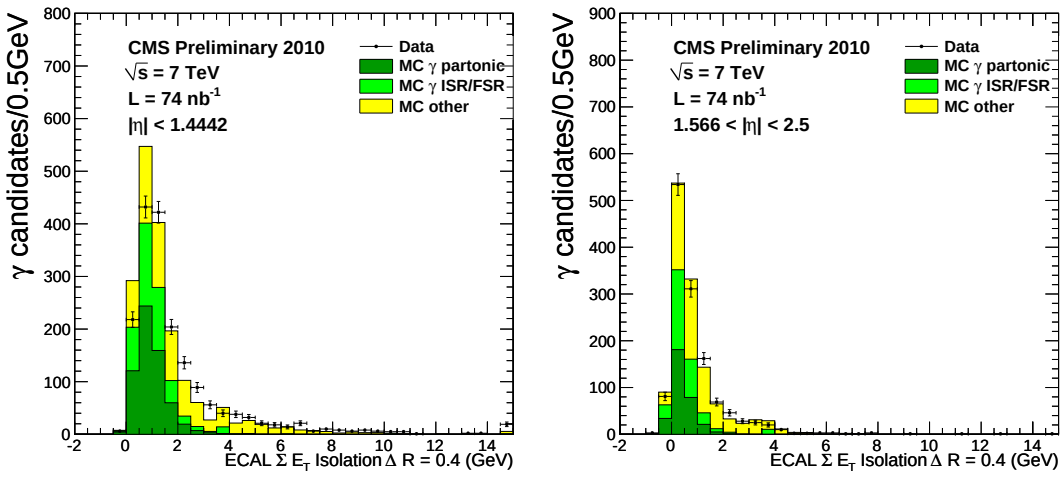

Figure 3.7: The ECAL isolation distributions for data and Monte Carlo simulation. The Monte Carlo results are normalized separately for each plot to the number of entries in the data histogram [16].

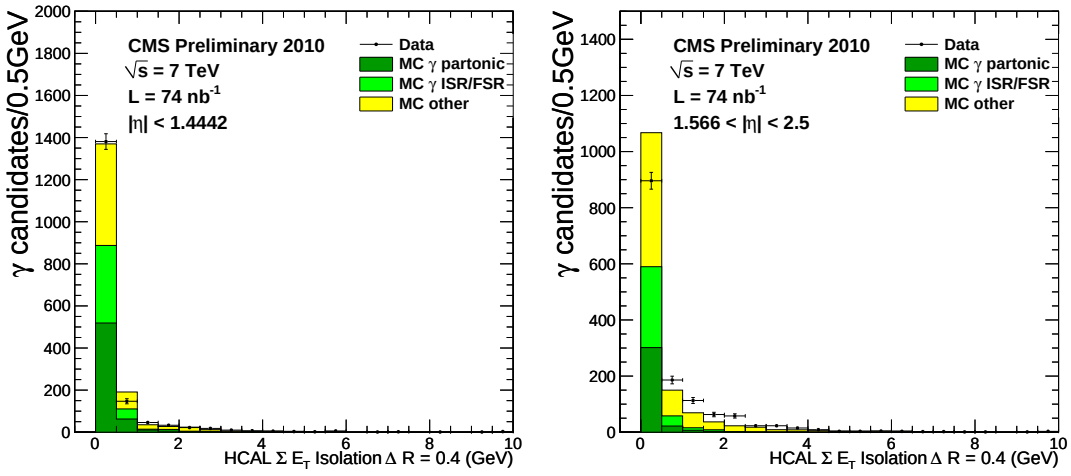

Figure 3.8: The HCAL isolation distributions for data and Monte Carlo simulation. The Monte Carlo results are normalized separately for each plot to the number of entries in the data histogram [16].

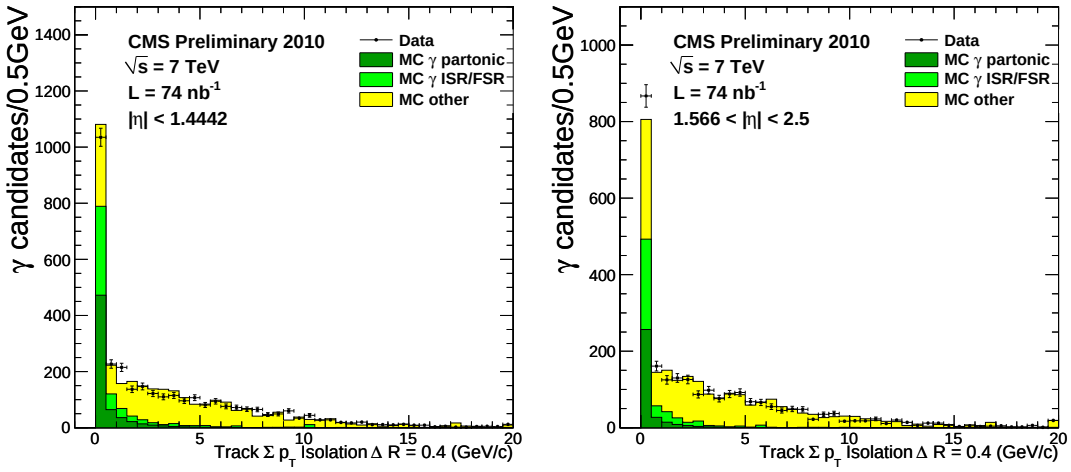

Figure 3.9: The track isolation distributions for data and Monte Carlo simulation. The Monte Carlo results are normalized separately for each plot to the number of entries in the data histogram [16]

3.5.4 Photon Conversion

Photon conversions are identified by an electron-positron pair having a conversion vertex. Their closest approach distance is short). The CMS standard tracking reconstruction is optimized for tracks coming from the primary interaction vertex with

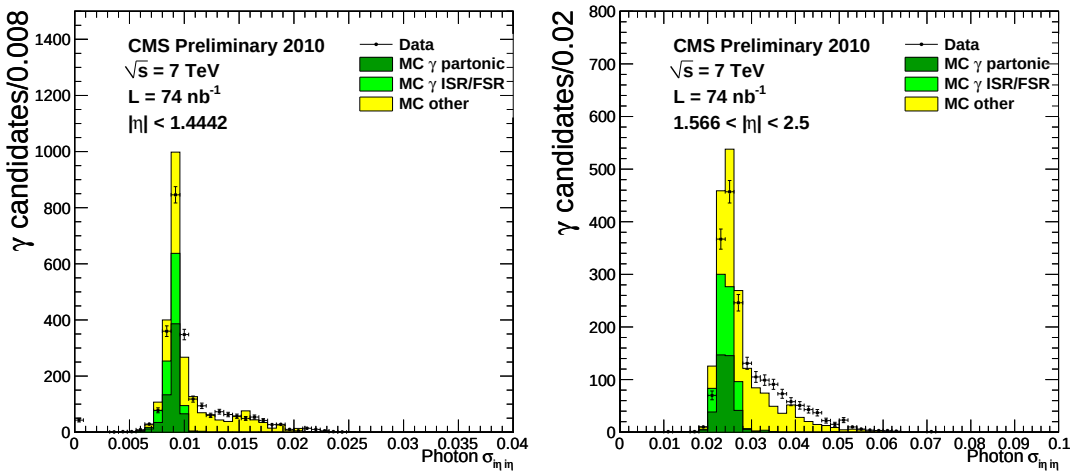

Figure 3.10: The shower shape distributions for data and Monte Carlo simulation. The Monte Carlo results are normalized separately for each plot to the number of entries in the data histogram [16].

pattern recognition starting from seeds found in the pixel detector. This method is not suitable for reconstructing the conversion tracks which originate from conversion points displaced from the primary interaction vertex.

A new tracking technique is developed [60]. In this approach, a predicted track path is found from the ECAL energy deposits (basic cluster) and the origin of the CMS reference frame. Pairs of hits are sought in the two outermost layers of the tracker in a small window from the hypothesis tracks. The search is extended to the third layer if no hit is found in the two outermost layers. If a compatible hit exists in these layers, the predicted track state is updated, taking this hit as the starting point. The search continues moving inward to the next layer until another hit is found. Using pattern recognition and trajectory building, seed tracks are formed from these pairs of hits. The initial seeds are transformed into a set of trajectory candidates (limited to 5 in order to avoid large combinatorics). The result of the inward tracking step is a list of tracks and only the opposite-charge pair with largest number of reconstructed hits are kept for the next step, outward tracking. In this

step, these tracks are used for the outward seed and track finding procedure. The tracks are built again from their innermost hit, assumed to be e^+e^- pair crossing point, and the ECAL basic cluster positions.

A photon conversion features a pair of oppositely charged tracks originating from the same point where the conversion happens (called conversion vertex). Thus, the angular separations between two tracks at the conversion vertex in the transverse plane ($\Delta\phi$) and longitudinal plane ($\Delta cot\theta$) are used for conversion identification. Requirement on χ^2 of the vertex fit is needed to ensure the quality of the conversion finding. Figure 3.11 shows these variables in the 7 TeV data.

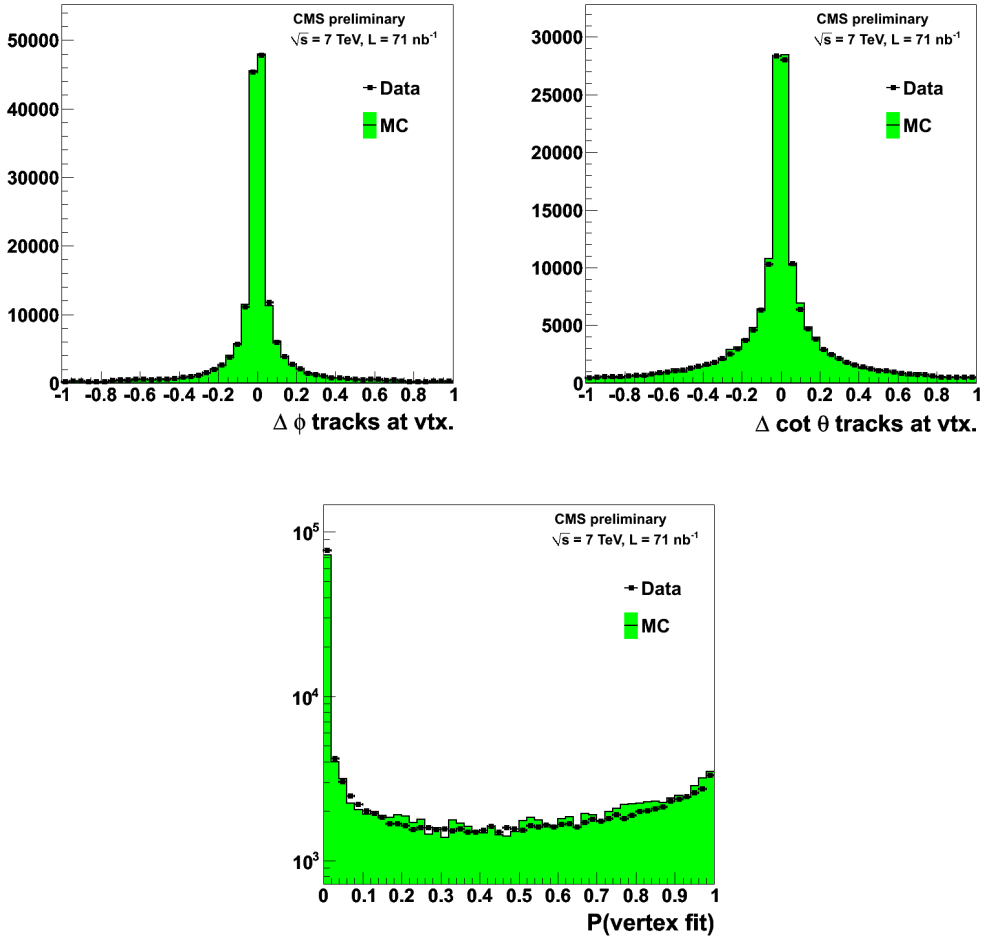

Figure 3.11: Conversion identification variables [16]

3.5.5 Electron Reconstruction

An electron candidate is a supercluster matched with a track. In contrast to photons, the electron's energy is measured from the supercluster in order to recover lost bremsstrahlung energy. Two complementary tracking algorithms in the track seeding generation are used ECAL driven [61] and tracker driven. The ECAL driven methods is optimized for an isolated electron with p_T in the range of electron from Z and W decays and down to ∼5 GeV. The tracker driven method performs better for low p_T electrons and electrons inside jets. The track reconstruction uses a Gaussian sum filter (GSF) algorithm which is optimized for electron tracks with long non-Gaussian tails in the energy loss distribution [62]. The GSF algorithm is built on a specific modeling of the electron energy loss and fitted (weighted sum of Gaussian distributions). Thus, it can adapt the change of curvature of the electron tracks and measures the track momentum at both track ends without a bias. Electrons are classified as [61]:

- "golden": a collection of low bremssstrahlung electrons with a reconstructed track well matching a supercluster
  - a supercluster formed by a single cluster (i.e. without observed bremsstrahlung sub-cluster)
  - E/p >0.9
  - f_{brem} <0.5
- "big brem": electrons with high bremsstrahlung fraction but no evidence of energy loss effects:
  - a supercluster formed by a single cluster,

  - E/p >0.9
  - f_{brem} >0.5

- "showering", or electrons with energy pattern highly affected by bremsstrahlung losses:
  - a supercluster formed by a single cluster not falling into the "golden" or "big brem" classes, or a supercluster formed by several subclusters.

$f_{brem} = (p_{in} - p_{out})/p_{in}$ where p_{in} and p_{out} are the track momenta at the innermost and outermost points. Furthermore, there are "crack" electrons which have their supercluster's starting crystal close to an η boundary between ECAL modules, or between ECAL barrel and endcaps. The classification is used to improve the electron momentum measurement. For a cut-based analysis, different cuts are designed for each electron class. The electron selection can be based on a matching between a track and a supercluster, and ratios between the electron's energy and momentum at the innermost or outermost point of the track. Shower shape and isolation variables are also used. Figure 3.12 shows the p_T and η distribution in minimum bias events at 7 TeV.

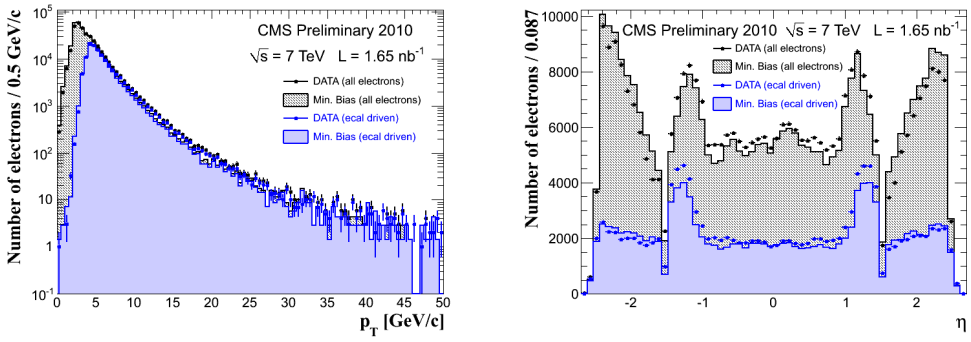

Figure 3.12: p_T and η distribution of electron [17]

Chapter 4

Analysis

The search for large extra dimensions in the diphoton channel are described in this chapter. We measure the invariant mass spectrum of photon pairs in data and look for an excess of events over the SM predictions at high masses due to the production of gravitons decaying to two photons. The high mass region is called the signal region since the LED signatures, if they exist, are present in this region. The main sources of backgrounds come from the SM diphoton, photon+jet and dijet processes. From the background studies at the signal region, the SM diphoton background is the most dominant background followed by the photon+jet background. The dijet process contributes the smallest fraction of the total background. The SM diphoton background is estimated in Monte Carlo simulation while photon+jet and dijet backgrounds are measured by data-driven methods. The Drell-Yan background, where two electrons are misidentified as photons, is negligible.

This chapter starts with the description of the data and samples used in this analysis in Section 4.1. Next, we discuss the optimization of kinematic cuts to ob-

tain the best sensitivity for the LED signals in Section 4.2. The event selection, its efficiency and the corresponding jet-faking-photon rate are described in Section 4.3, Section 4.5 and Section 4.6, respectively. Finally, the method of background estimation is discussed in Section 4.7.

4.1 Data and Monte Carlo Samples

About 36 pb^{-1} of data collected in the 2010 run are used in this analysis. The reconstruction software was updated regularly during the data collection to have the latest improvement and up-to-date running conditions. Between data taking periods (often during a technical stop of the LHC), collected data are reprocessed in order to bring them to the most up-to-date reconstruction release. The data quality is certified offline. We include only data in luminosity sections, where the LHC machine and the CMS detector are in good operation. The following data sets are used:

- EG (Egamma) data set: `/EG/Run2010A-Nov4ReReco_v1/RECO`; lumi: 3.18 pb^{-1}, run range: 136035-144114
- Photon data set: `/Photon/Run2010B-Nov4ReReco_v1/RECO`; lumi: 32.96 pb^{-1}, run range: 146428-149294

These data sets are first collected in two data taking periods, Run2010A and Run2010B. After that they are reprocessed in `CMSSW_3_8_6` release in November, 2010. The EG data set comes from the HLT paths triggering on high transverse momentum electromagnetic objects (superclusters). In Run2010B, the luminosity is

increased significantly. The photon data set is selected by tighter HLT photon filters to enrich well-defined photon candidates while the rate is maintained.

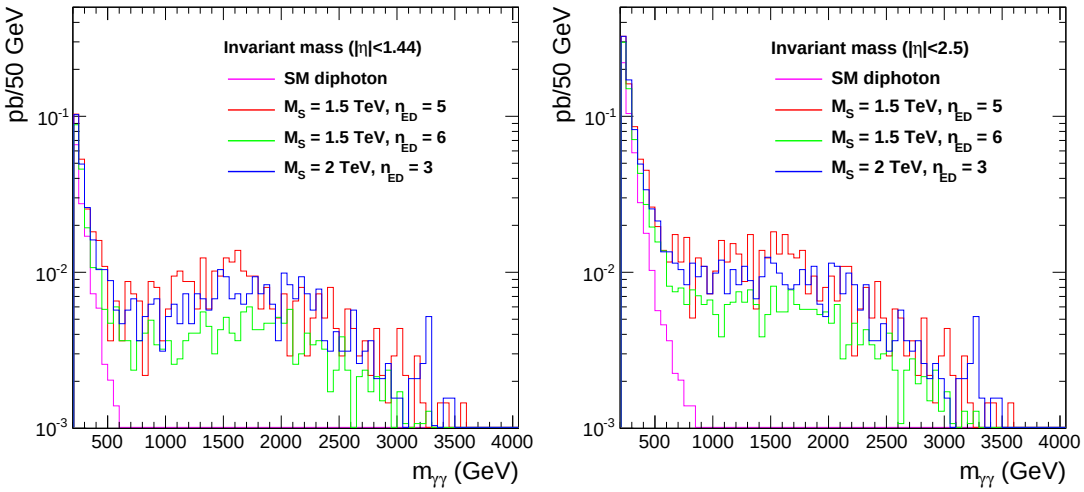

Figure 4.1: Invariant mass distributions of the SM diphotons and some ADD signals. The invariant masses are plotted for EB (left) and EB+EE (right) regions

The generator `PYTHIA` [63] is used to produce samples for the SM diphoton study. `PYTHIA` contains a library of hard processes and models for initial- and nal-state parton showers, multiple parton-parton interactions, beam remnants, string fragmentation and particle decays [64]. Both Born and Box process are included in the sample generation. In order to increase the statistics at high $\widehat{p}_T$ phase space, where $\widehat{p}_T$ is the transverse momentum of the hard scattering, the event generation is done in separate sub $\widehat{p}_T$ phase spaces. Below are the Born and Box samples generated in different sub $\widehat{p}_T$ phase spaces from 10 GeV to infinity. The σ stands for the cross section.

- `/DiPhotonBorn_Pt10to25/Summer10-START36_V9_S09-v1/GEN-SIM-RECODEBUG`, $\widehat{p}_T$ = 10-25 GeV, σ = 236.4 pb
- `/DiPhotonBorn_Pt25to250/Summer10-START36_V9_S09-v1/GEN-SIM-RECODEBUG`, $\widehat{p}_T$ = 25-250 GeV, σ = 22.37 pb

- /DiPhotonBorn_Pt25toInf/Summer10-START36_V9_S09-v1/GEN-SIM-RECODEBUG, $\widehat{p}_T$ = 25-∞ GeV, $\sigma = 8.072 \times 10^{-3}$ pb
- /DiPhotonBox_Pt10to25/Summer10-START36_V9_S09-v1/GEN-SIM-RECODEBUG, $\widehat{p}_T$ = 10-25 GeV, σ = 358.2 pb
- /DiPhotonBox_Pt25to250/Summer10-START36_V9_S09-v1/GEN-SIM-RECODEBUG, $\widehat{p}_T$ = 25-250 GeV, σ = 12.37 pb
- /DiPhotonBox_Pt250toInf/Summer10-START36_V9_S09-v1/GEN-SIM-RECODEBUG, $\widehat{p}_T$ = 250-∞ GeV, $\sigma = 2.08 \times 10^{-4}$ pb

We also use PYTHIA to generate photon+jet samples. These samples are used in the background estimation.

- /PhotonJet_Pt30/Summer10-START36_V9_S09-v1/GEN-SIM-RECODEBUG
  cross section: 2.007×10^4 pb^{-1}
- /PhotonJet_Pt80/Summer10-START36_V9_S09-v1/GEN-SIM-RECODEBUG
  cross section: 556.5 pb
- /PhotonJet_Pt170/Summer10-START36_V9_S09-v1/GEN-SIM-RECODEBUG
  cross section: 24.37 pb
- /PhotonJet_Pt300/Summer10-START36_V9_S09-v1/GEN-SIM-RECODEBUG
  cross section: 1.636 pb

We use the SHERPA generator version 1.1.2 to generate the ADD signal samples. SHERPA implements the ADD model based on the helicity formalism of spin-2 particles [65]. In order to take into account for the interference between SM diphoton production and ED diphoton effects, Sherpa generates both processes together. We

generate several signal samples with various values of n_{ED} and M_S. The cross sections of the pure ED effect after subtracting the SM term are also shown in Table 4.1. We also generate a sample with $M_S = 100$ TeV, which effectively turns off virtual graviton effects, while retaining SM diphoton production.

	Positive Interference (HLZ)		Negative Interference (Hewett)	
Sample	σ (pb)	$\sigma \times \mathcal{A}$ (pb)	σ (pb)	$\sigma \times \mathcal{A}$ (pb)
$M_S = 1.2$ TeV, $n_{\mathrm{ED}} = 5$	7.31	3.19	—	—
$M_S = 1.5$ TeV, $n_{\mathrm{ED}} = 2$	3.32	7.14×10^{-1}	1.90	3.04×10^{-1}
$M_S = 1.5$ TeV, $n_{\mathrm{ED}} = 5$	2.16	3.34×10^{-1}		
$M_S = 1.5$ TeV, $n_{\mathrm{ED}} = 6$	1.69	1.82×10^{-1}		
$M_S = 1.5$ TeV, $n_{\mathrm{ED}} = 7$	1.47	1.02×10^{-1}		
$M_S = 2$ TeV, $n_{\mathrm{ED}} = 2$	1.35	6.06×10^{-2}	1.12	2.79×10^{-2}
$M_S = 2$ TeV, $n_{\mathrm{ED}} = 3$	2.05	2.98×10^{-1}		
$M_S = 2$ TeV, $n_{\mathrm{ED}} = 4$	1.32	6.78×10^{-2}		
$M_S = 2$ TeV, $n_{\mathrm{ED}} = 7$	1.11	1.36×10^{-2}		
$M_S = 2.5$ TeV, $n_{\mathrm{ED}} = 2$	1.15	2.02×10^{-2}	1.06	1.07×10^{-2}
$M_S = 2.5$ TeV, $n_{\mathrm{ED}} = 3$	1.24	4.54×10^{-2}		
$M_S = 2.5$ TeV, $n_{\mathrm{ED}} = 4$	1.11	1.52×10^{-2}		
$M_S = 2.5$ TeV, $n_{\mathrm{ED}} = 7$	1.07	1.91×10^{-3}		
$M_S = 3$ TeV, $n_{\mathrm{ED}} = 2$	1.10	7.75×10^{-3}	1.05	7.04×10^{-3}

Table 4.1: Total cross section and cross section × acceptance for different samples. Cross sections include SM diphoton production in addition to ADD phenomena. The acceptance criteria are two generator-level photons with $E_T > 30$ GeV and $|\eta| < 1.442$ that form an invariant mass $M_{\gamma\gamma} > 500$ GeV. The first set of cross sections (columns two and three) have positive interference between SM and ADD signals, while the second set (columns four and five) have negative interference. The second set is used in the Hewett convention of virtual graviton production. No NLO K-factor is applied.

4.2 Signal Optimization

We optimize our selection criteria to minimize the expected 95% confidence level limit on the cross section for the ADD model with parameters close to the expected sensitivity. The process of calculating the expected limit is described in detail in Section 5.3. For the optimization, we ignore any systematic uncertainties. We opti-

mize based on an estimation of the diphoton rate from MC and the jet background from data.

We optimize based on two variables: the invariant mass of the photon pairs, and the maximum allowed $|\eta|$ of the individual photons. Virtual KK graviton production will evince itself as a contiuum spectrum above the expected SM background at high invariant mass. The signal is also more central than the SM (see Figure 4.2). To find the best choice of selection values, we first fix the invariant mass requirement at $M_{\gamma\gamma} > 400$ GeV, and then find the optimal $|\eta|$ requirement. Once this is found, we fix the $|\eta|$ requirement, and measure the optimal $M_{\gamma\gamma}$ cut. This iterative process helps us converge on an optimal point without needing to optimize on both variables simultaneously.

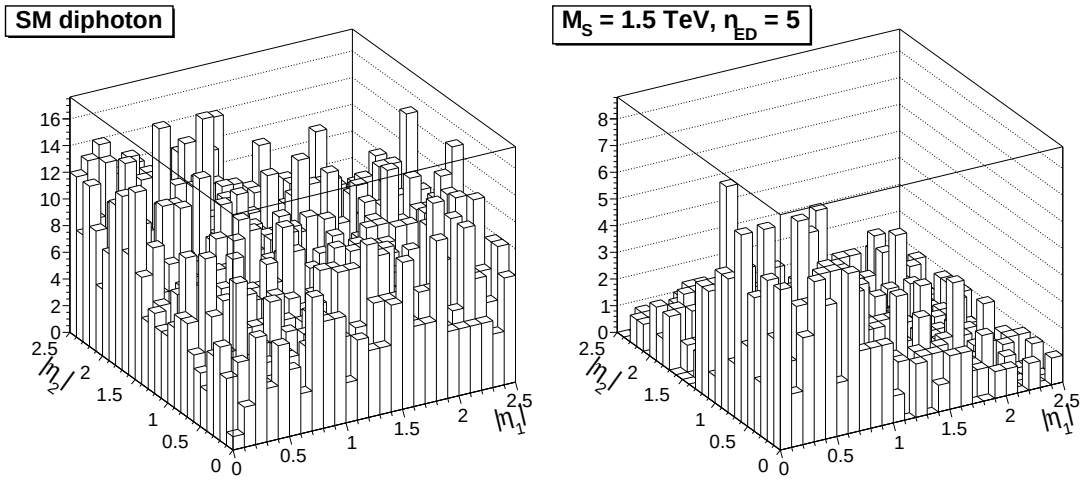

Figure 4.2: Pseudo-rapidity distributions of two photons for SM diphoton (left) and ADD signals with $M_S = 1.5$ TeV $n_{ED} = 5$

.

Figure 4.3 shows both steps of optimization process. The plot on the left is the expected 95% confidence level limit on the signal cross section as a function of $|\eta|$ with $M_{\gamma\gamma} > 400$ GeV for a variety of choices for M_S and the number of ED. The normalization is arbitrary since we are looking only for local minima. We choose

$|\eta| < 1.442$, since this conveniently corresponds to both the approximate location of the optimal cut point and the location of the gap between the ECAL barrel and endcap.

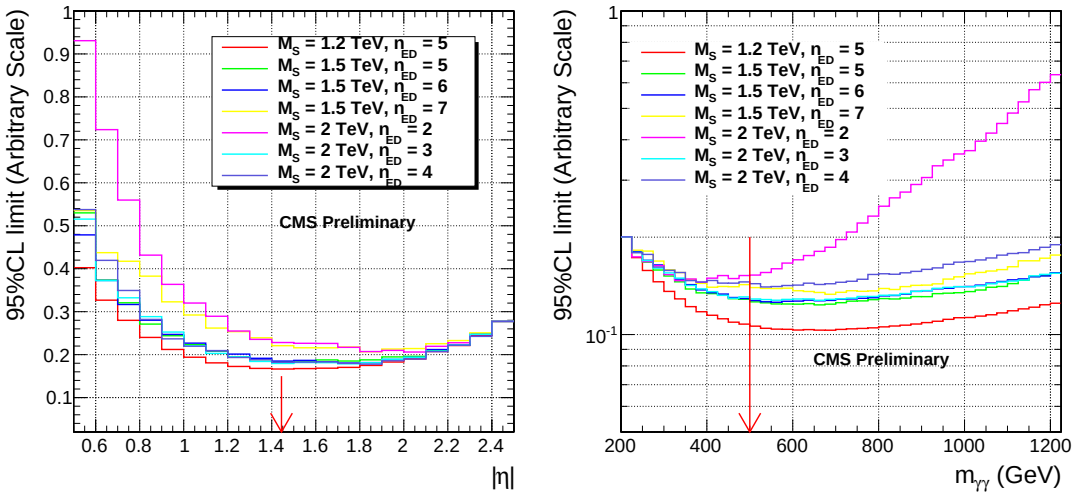

Figure 4.3: Expected 95% limit on the cross section for various ED models. Left: the limit as a function of $|\eta|$ with $M_{\gamma\gamma} > 600$ GeV. Right: the limit as a function of $M_{\gamma\gamma}$ with $|\eta| < 1.442$.

After the optimum $|\eta|$ cut has been chosen, we focus on the invariant mass threshold. This is shown in the right pane in Figure 4.3. Based on this plot, we choose to require $M_{\gamma\gamma} > 500$ GeV, as this is the optimal point for much of the parameter space.

4.3 Event Selection

The final goal of the event selection is to select a high-purity diphoton candidate sample without losing hypothetical new physics signals. At first, the events are selected by the CMS 2-level trigger systems described in Section 2.2.6. The generic double-photon trigger paths in Table 4.2 are used. At least one good vertex within $|z| < 24$ cm and $d_0 < 2$ cm is required, where z is the z-coordinate of the vertex and

d_0 is the distance from the vertex to the beam line. The next step is to select events containing two high-transverse-momentum photons. Table 4.3 lists the kinematic and the photon identification cuts. The η cut is equivalent to restricting two photons to the ECAL barrel. As discussed in Section 4.2, this choice is a good compromise between the search sensitivity and the need to understand complicated backgrounds in the ECAL endcap.

Run range	Trigger name	Threshold (GeV)
136033-141881	$HLT\_DoublePhoton10\_L1R$	10
141882-144114	$HLT\_DoublePhoton15\_L1R$	15
144115-148058	$HLT\_DoublePhoton17\_L1R$	17
148059-149294	$HLT\_DoublePhoton22\_L1R\_v1$	22

Table 4.2: HLT trigger path

Cuts	Tight value
E_T	< 30 GeV
$\|\eta\|$	< 1.4442
EcalIso	$< 4.2 + 0.006 \cdot p_T$ GeV
HcalIso	$< 2.2 + 0.0025 \cdot p_T$ GeV
TrkIso	$< 2 + 0.001 \cdot p_T$ GeV
Pixel seed veto	false
$\sigma_{i\eta i\eta}$	0.013

Table 4.3: Photon selection. The η cut is defined from the sensitivity optimization presented in Section 4.2

4.4 Anomalous Energy Deposit Cleaning

Anomalous energy deposits are observed in the ECAL barrel due to direct ionization of the avalanche photodiode (APD) sensitive volumes by highly ionizing particles produced during proton-proton collisions [18]. Because, these energy deposits are often observed in a single ECAL crystal, they are called "spikes". They are found at the rate of ~ 1 in 10^3 minimum bias events.

The rejection of those spikes is based on topological and timing characteristics. A spike appears as a high-energy deposition in a single crystal surrounded by quiet adjacent crystals (see Figure 4.4). The "Swiss Cross" variable (S) defined as $1 - E_4/E_1$, where E_1 is the energy of the seed crystal (a crystal with highest energy in a cluster of a photon) and E_4 is the total energy of four crystal adjacent to the seed crystal, is used in spike cleaning. A cut at $S < 0.95$ reject 99.2% spikes with $E_T > 10$ GeV [18]. A genuine signal pulse from a photon has a time constant consistent

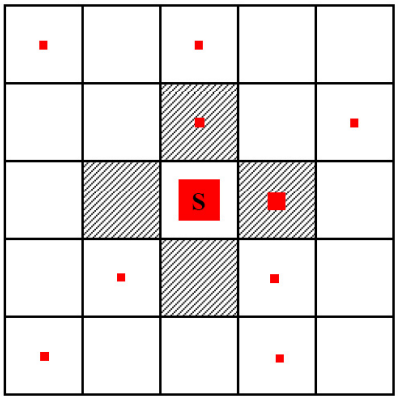

Figure 4.4: A spike event in the ECAL. Only the seed crystal (S) has a significant energy deposit. Energy deposits in the four adjacent crystals (hatched) are used in the spike rejection.

with the convolution of the time profile of light emission from the lead tungstate crystals (80% of light emitted in 25 ns) and the response of the front-end electronics (shaping time $\tau \sim 40$ ns). In contrast, the signal pulse from a spike contains only the electronic shaping time since the spike energy deposit happens inside the APD. This difference in shape produces a bias in the measured time of the signal pulse when the anomalous energy deposits are reconstructed with the expected pulse shape for scintillation light [18]. A pulse is declared out-of-time if the difference between the measured and expected time is greater than 5 standard deviations [18].

Figure 4.5 shows the S and the signal timing distributions of photon. A pronounced peak ~ 1 is seen in S distribution for data. The timing distribution shows many out-of-time photons. Both the S cut and the timing cut are applied when

processing data to reject automatically spike photons.

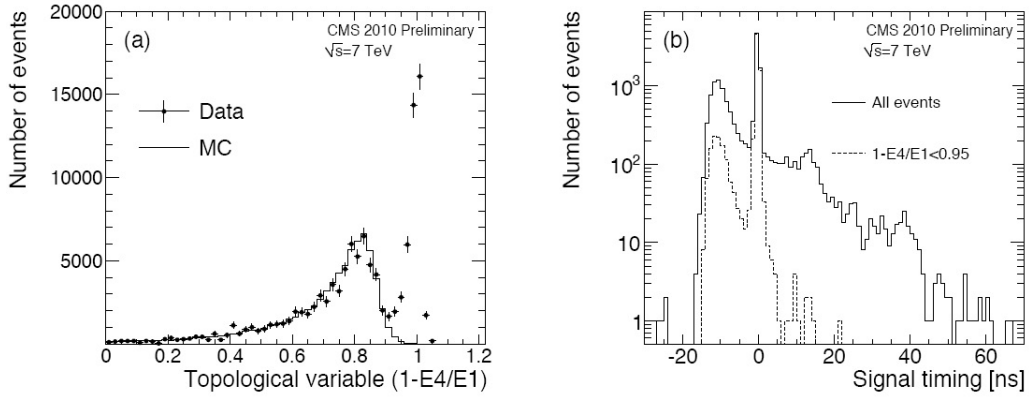

Figure 4.5: (a) Distribution of the Swiss Cross topological variable (1-E_4/E_1) for the highest energy deposit each event for data and simulation ($\sqrt{s}$ = 7 TeV); (b) Reconstructed time corresponding to the maximum of the signal pulse for the highest energy deposit in each event [18]

4.5 Photon Efficiency

The photon efficiency is measured using the MC photon+jet samples. A generator-level photon is spatially matched to a reconstructed photon. If a reconstructed photon is found, the photon identification efficiency is calculated. The MC matching is necessary since a photon can be reconstructed from a electromagnetic fluctuation of a jet. Figure 4.6 shows the efficiency versus photon p_T and η in MC. The combined efficiency is flat in p_T and η and central at 90%. A 2% systematic uncertainty is assigned to account for a small variation of the efficiency. In order to correct for the difference between efficiency in MC and data, a scale factor is derived. Because of the similarity between photons and electrons, this scale factor for photons is similar to that of electron which is derived in $Z \rightarrow e^+e^-$ events using the tag-and-probe technique. The scale factor value is 1.010±0.012 with the uncertainty covering the difference between photons and electrons [66].

Another component of the photon efficiency is the efficiency of the pixel seed veto which is $96.6 \pm 0.5(\text{syst})\%$. This quantity is also estimated in MC, and its uncertainty is obtained by comparing different geometric configurations of the beam pipe and the pixel detector [67]. The total single photon efficiency for the selection in Table 4.3 is (87.8±2.3)% which can be turned into the diphoton reconstruction and identification efficiency of (77.1±4.0)%.

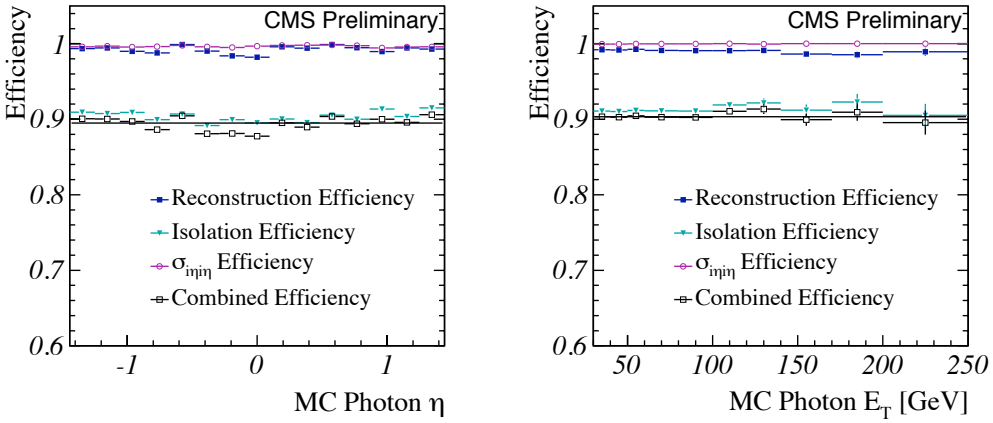

Figure 4.6: Reconstruction, $\sigma_{i\eta i\eta}$ cut, isolation, and combined efficiency as a function of p_T and η.

4.6 Jet-faking-photon Rate

A jet can misidentified as a "fake photon", especially when most of its energy is carried by electromagnetic decay particles, for example π_0. Although the jet-faking-photon rate (or photon fake rate for short) is small ($\sim 10^{-4}$), the contribution of the backgrounds coming from the SM processes associated with jets in the final state (e.g., dijets and photon+jets) to photon analysis can be significant due to the high cross section of those processes. In this section, a method to estimate the photon fake rate is described. The photon fake rate is derived from a photon dataset collected

by single photon trigger paths which contain very loose photons. In this dataset, the number of photons passing the tight selection in Table 4.3, N_T^{fake} and the number of photons passing the loose photon selection N_L^{fake} are found. The loose photon selection is defined as:

$E_T < 30$ GeV

$|\eta| < 1.4442$

$EcalIso < min(5 \times (4.2 + 0.006 \times p_T), 0.2 \times p_T)$

$HcalIso < min(5 \times (2.2 + 0.0025 \times p_T), 0.2 \times p_T)$

$TrkIso < min(5 \times (3.5 + 0.001 \times p_T), 0.2 \times p_T)$

AND inverting one of the identification variables

$EcalIso > (4.2 + 0.006 \times p_T)$ OR

$HcalIso > (2.2 + 0.0025 \times p_T)$ OR

$TrkIso > (3.5 + 0.001 \times p_T)$ OR

$\sigma_{i\eta i\eta} > 0.013$

where p_T is in GeV. The photon fake rate is defined as:

$$f_\gamma = \frac{N_T^{fake}}{N_L^{fake}}. \tag{4.1}$$

The denominator photon selection contains an inverted tight photon ID cut which is needed to reduce the contamination from direct photons. It can be seen that the fake rate is not exactly the probability of a fake photon to be recognized as a tight photon which is defined as:

$$p_\gamma = \frac{N_T^{fake}}{N_T^{fake} + N_L^{fake}} \tag{4.2}$$

However, those are related by

$$f_\gamma = \frac{p_\gamma}{1 - p_\gamma} \tag{4.3}$$

The tight photons observed in the data, N_T^{obs}, include both N_T^{fake}, which originated from jets and direct photons or real photons mostly from photon+jets processes.

The photon purity, P, which is the fraction of direct photons in N_T^{obs}, can be as high as 70% at p_T ∼80 GeV. The equation Eq. 4.1 is rewritten as:

$$f_\gamma = \frac{N_T^{obs} \times (1 - P)}{N_L^{fake}} \tag{4.4}$$

The contribution of genuine photons to the denominator in Eq. 4.4 is negligible due to the inverted tight photon ID cut applied.

4.6.1 Photon Purity

The photon purity is the fraction of prompt photons in the sample of interest. Here, the sample of interest contains the tight photons selected by the tight selection in Section 4.3. A template method is used. The prompt photon templates (the signal templates), and the fake photon template (the background templates) are provided as inputs. A binned likelihood fit is perform to find the best fit of those templates to data.

The shower shape template, $\sigma_{i\eta i\eta}$, is powerful in the signal-background separator. Therefore, the shower shape method is chosen to get the central values of the purity. Other template methods, the isolation sum and the conversion methods, are also considered as cross-checks and discussed later in this section. The prompt photon templates can be obtained from the photons associated with W or Z bosons in which the fake photons are reduced significantly by the W or Z selection. With insufficient events of those processes, we derive the real photon templates from Monte Carlo (MC) photon+jet samples. The background templates are derived in a background-enriched region given by inverting the track isolation requirement $2 + 0.001 \times p_T <$ TrkIso < 4 GeV. TrkIso is the track isolation defined in Section 3.5.3. There may be

correlation between the shower shape variable and the track isolation cuts used to define the background-enriched region. This correlation can affect the correctness in modeling the background templates at the signal region. The fit is performed by the `TFractionFitter` method of `ROOT`. The `TFractionFitter` is a standard likelihood fit using Poisson statistics. The results of the fit are presented in Figure 4.7.

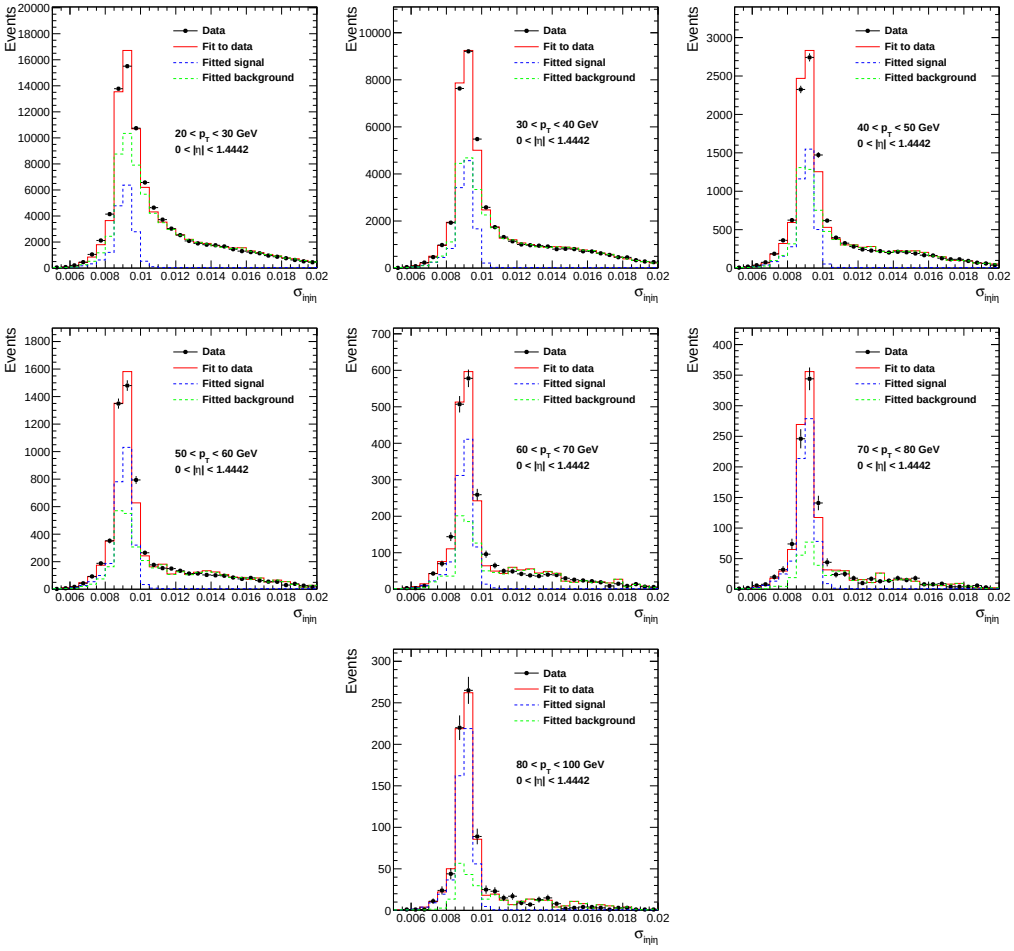

Figure 4.7: $\sigma_{i\eta i\eta}$ template fit.

The sum of photon isolation is defined as $Iso = Iso_{Ecal} + Iso_{Hcal} + Iso_{Trk}$. Here $Iso_{Ecal}, Iso_{Hcal}, Iso_{Trk}$ are the isolation variables in Ecal, Hcal and tracker, respectively. This variable is also good in signal-background separation and can be used in the template fitting. The signal templates are derived in MC while the

background templates are obtained from a nearby side-band region, $0.011 < \sigma_{i\eta i\eta} < 0.013$. The main drawback of this method is that the isolation is very sensitive to the pile-up effects (However, pile-up is small in the 2010 runs) and the sample used in the purity calculation is different from the sample of interest selected by tight selection. The pile-up effects are not well-simulated in the MC simulation so the difference between a MC signal template and a true data template can be significant. The later drawback implies that the calculated purity and the purity in the sample of interest may not be the same. Figure 4.8 shows the fit results.

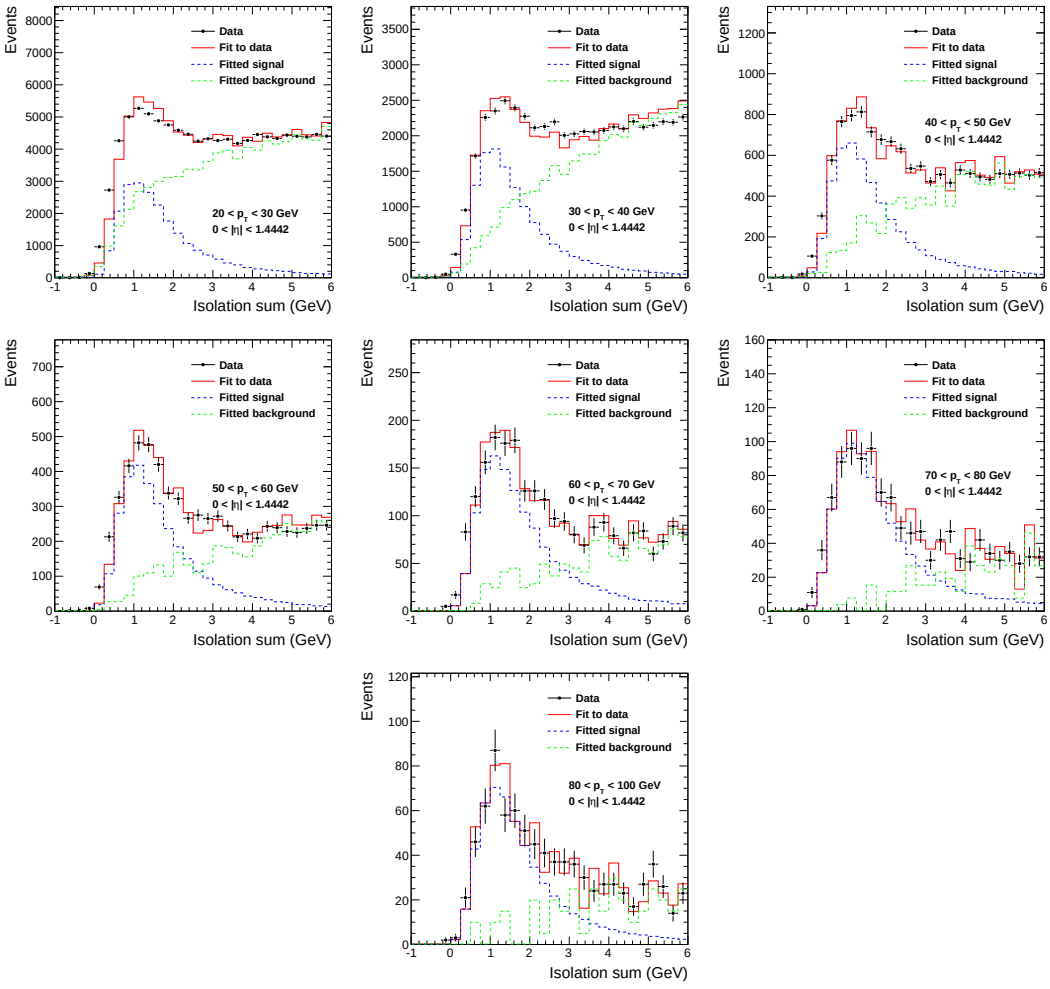

Figure 4.8: Isolation sum template fit.

Our final method is to use converted photons. Two photons are selected by

requiring that two, oppositely charged tracks associated with corresponding electromagnetic clusters form a conversion vertex: $|\Delta\cot(\theta)| < 0.05$ and $|\Delta\phi_{vtx}| < 0.1$. These photons are required to pass the tight selection. A side-band region of $0.011 < \sigma_{i\eta i\eta} < 0.013$ is used to get the background templates. Figure 4.9 shows the result of the conversion fits.

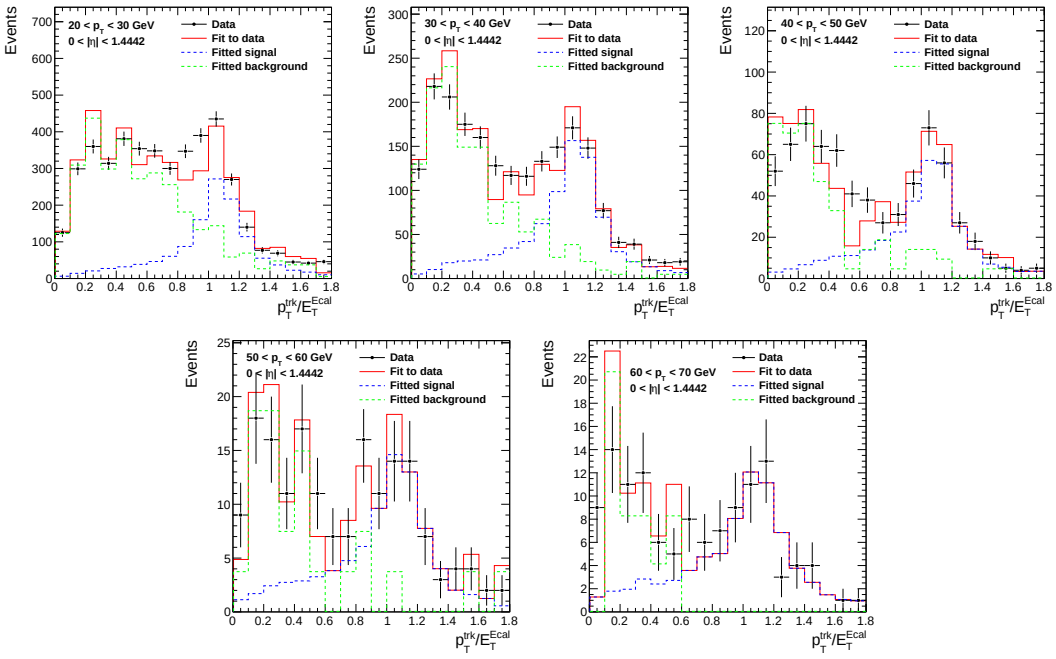

Figure 4.9: Conversion template fit.

4.6.2 Corrected Fake Rate

By correcting the measured fake rate for the purity as a function of photon E_T, we get the rates shown in Figure 4.10 for each of the template methods. Table 4.4 shows those rates in numbers. We see that the fake rates from the isolation and the conversion methods are within 20% relative with respect to the central values from the $\sigma_{i\eta i\eta}$ method.

E_T bin (GeV)	Shower shape	Isolation sum	Conversion
20-30	0.532 ± 0.009	0.491 ± 0.008	0.535 ± 0.027
30-40	0.183 ± 0.003	0.177 ± 0.003	0.205 ± 0.010
40-50	0.128 ± 0.003	0.114 ± 0.003	0.140 ± 0.011
50-60	0.076 ± 0.002	0.067 ± 0.002	0.097 ± 0.013
60-70	0.056 ± 0.002	0.044 ± 0.002	0.068 ± 0.009
70-80	0.033 ± 0.002	0.027 ± 0.001	-
80-100	0.030 ± 0.002	0.030 ± 0.002	-

Table 4.4: Fake rates from shower shape, isolation sum and conversion methods

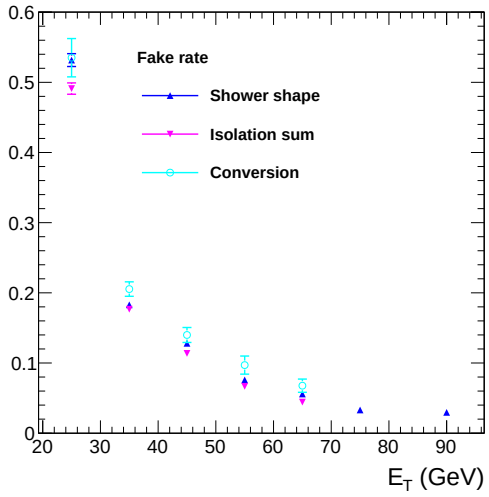

Figure 4.10: Photon fake rate using various methods of correcting for the real photon contamination.

4.6.3 Fake Rate and Trigger

The single photon triggers are used to collect the samples used in Section 4.6.2. This section discusses the choice of triggers. The non-isolated HLT triggers in which there is no isolation requirement applied to photon trigger objects are chosen. The fake rate for each trigger with thresholds at 30, 50 and 70 GeV are shown in Figure 4.11. It can be seen that the fake rate is lower below the thresholds and above the trigger thresholds all fake rates are in good agreement. Therefore, the 30, 50 and 70 GeV triggers are used for estimating the fake rate in p_T range 30-50, 50-70 and above 70, respectively. The fake rates are also derived from the samples selected by jet

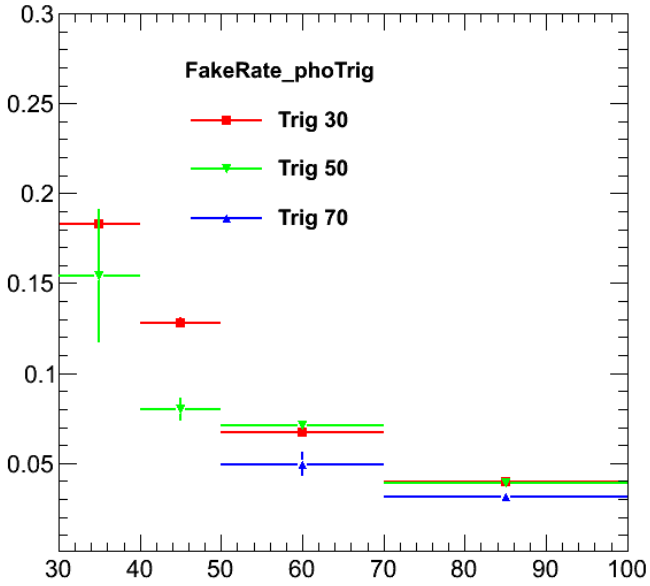

Figure 4.11: Photon fake rates from photon triggers with thresholds of 30 GeV (red), 50 GeV (green), and 70 GeV (blue).

or muon triggers. There are a small discrepancies between the results from those triggers. The fake rates of different triggers are then combined in a common fit by a function of E_T:

$$p_0 + \frac{p_1}{x^{p_2}} \tag{4.5}$$

The fit results are shown in Figure 4.12. The coefficients found from a best fit are:

$$p_0 = 0.01598, p_1 = 2431.92, p_2 = 2.67771. \tag{4.6}$$

Figure 4.12 also represents the ratio of observed fake rates and the best fit function of combined fake rates. From that, a 20% systematic error is assigned to cover the variation of observed fake rates.

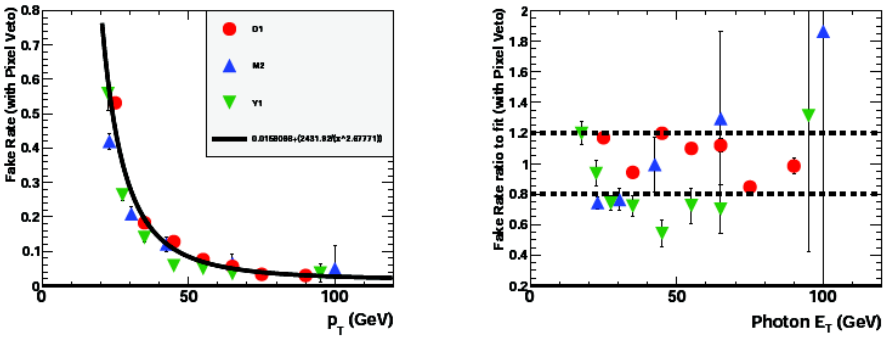

Figure 4.12: Photon fake rates from photon (red), muon (blue) and jet (green) triggers and their ratios to the best fit function.

4.7 Backgrounds

The main sources of backgrounds come from SM diphoton production, and the QCD processes with jets in the final states (dijets, photon+jets). The SM diphoton background is irreducible since the events always pass the photon selection and contribute significantly to the total background especially in the signal region (the high end of the diphoton invariant mass spectrum). This type of background is estimated in MC and described in Section 4.7.1. The QCD background can be estimated in a data-driven manner using the photon fake rate, the rate at which a jet fakes as a photon. This background is less important than the diphoton background in the signal region given. Details are given in Section 4.7.2.

4.7.1 SM Diphotons

The SM diphoton background is estimated in MC using the PYTHIA generator and the full detector simulation by GEANT4. Both contributions from Born and Box processes are taken into account. Since these are the tree-level LO contributions, the K-factor, which is the ratio between LO and NLO cross sections, is applied as

a scale factor to the diphoton background prediction from PYTHIA. In this analysis, we apply a conservative K-factor of 1.3 used by Tevatron experiments. In principle, K-factor depends on the center-of-mass energy of hadron-hadron collisions and the invariant mass of the diphotons.

We use a dedicated program for diphoton cross section calculation, called DIPHOX [68], to study the K-factor of pp collision at 7 TeV. All the LO and NLO diagrams of direct and fragmentation processes described in Section 4.5 are implemented in DIPHOX. In order to be consistent with photon selection, we limit the η range within $|\eta| < 1.4442$. Table 4.5 summarizes the parameter setup. Figure 4.13 shows the LO and NLO cross sections and the K-factor as the functions of the diphoton invariant mass.

Name	Value
PDF	CTEQ6
Type of fragmentation functions	402
Initial state factorisation scale	0.5 cm
Final state factorisation scale	0.5 cm
Renormalization scale	0.5 cm
$\|\eta\|$	< 1.4442
p_T	> 30 GeV
Radius of isolation cone	0.4

Table 4.5: The parameter setup in DIPHOX for the cross section calculation

4.7.2 Dijet and Photon+jet

Utilizing the photon fake rate, the dijet and photon+jet backgrounds (QCD background) can be estimated by the following method. The events with two photons are considered. Among the total number of those events, there are $N_{\gamma\gamma}$ events with two real photons, N_{jj} with two fake photons and $N_{\gamma j}$ with one real and one fake photon. If the transverse momenta of photons denoted as x and y, the numbers of events

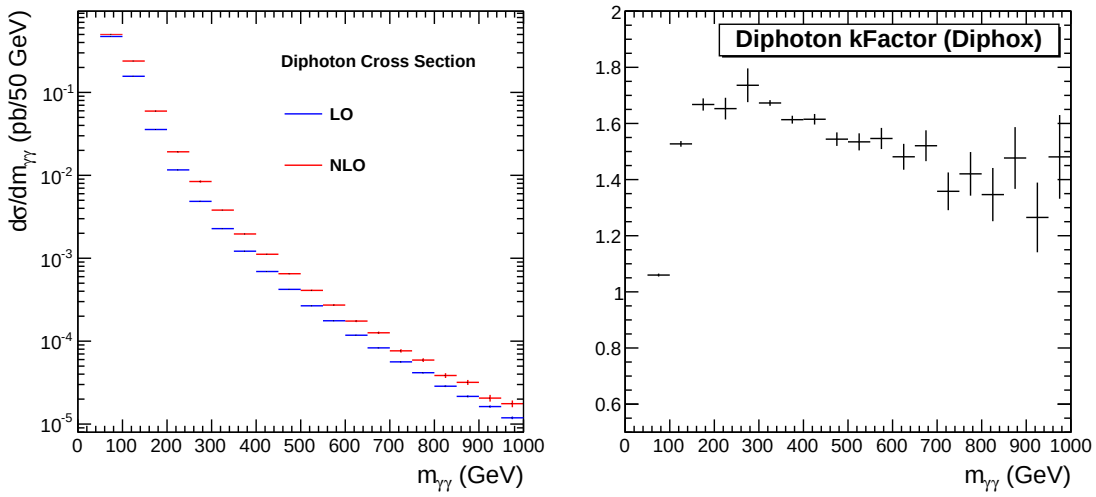

Figure 4.13: The diphoton cross sections (left) and the K-factor (right) from DIPHOX

in each category are $N^{xy}_{\gamma\gamma}$, N^{xy}_{jj}, $N^{xy}_{\gamma j}$ and $N^{xy}_{j\gamma}$. The ordering of subscripts decides which photon has transverse momentum x or y. That is why two combinations for the case of one real and one fake photon are needed. An important thing is that those numbers of events are not known because the real and fake photons are mixed undistinguishable in data. What is observed instead are the tight (denoted T) and the fakeable (denoted F) photons. Therefore, the observed diphoton events are N^{xy}_{TT}, N^{xy}_{FF}, N^{xy}_{TF}, N^{xy}_{FT} corresponding to the number of diphoton events with two tight, two fakeable and one tight and one fakeable photons, respectively. Again, the ordering of the subscript indicates which photons has $p_T = x$ or $p_T = y$. Recalling that p_x and p_y are the probability of a photon identified as a tight photon, one can write these equations:

$$N^{xy}_{FF} = N^{xy}_{jj}(1-p_x)(1-p_y), \tag{4.7}$$

$$N^{xy}_{FT} = N^{xy}_{jj}(1-p_x)p_y + N^{xy}_{j\gamma}(1-p_x), \tag{4.8}$$

$$N^{xy}_{TF} = N^{xy}_{jj}p_x(1-p_y) + N^{xy}_{\gamma j}(1-p_y), \tag{4.9}$$

$$N^{xy}_{TT} = (N^{xy}_{jj}p_xp_y + (N^{xy}_{j\gamma}p_x + N^{xy}_{\gamma j}p_y) + (N^{xy}_{\gamma\gamma}). \tag{4.10}$$

Solving these equations, the number of diphoton events with two tight photons, which is the background to the analysis, can be expressed by observables and probability of identifying a tight photon:

$$\begin{aligned} N_{TT}^{xy} &= \left(N_{FF}^{xy} \frac{p_x p_y}{(1-p_x)(1-p_y)} \right) \\ &+ \left(-2N_{FF}^{xy} \frac{p_x p_y}{(1-p_x)(1-p_y)} + N_{FT}^{xy} \frac{p_x}{1-p_x} + N_{TF}^{xy} \frac{p_y}{1-p_y} \right) \\ &+ (N_{\gamma\gamma}^{xy}) \end{aligned}$$

The terms in parentheses correspond to the background contributions from di-jet, photon+jet and diphoton, respectively. Finally, using Eq. 4.3, we rewrite the expression in term of fake rate:

$$N_{TT}^{xy} = (N_{FF}^{xy} f_x f_y) + (-2N_{FF}^{xy} f_x f_y + N_{FT}^{xy} f_x + N_{TF}^{xy} f_y) + (N_{\gamma\gamma}^{xy}). \tag{4.11}$$

Chapter 5

Results and Conclusions

5.1 Data and Background Prediction

Figure 5.1 shows the diphoton invariant mass spectrum from data and background estimations. There is no excess of data events over the SM background estimations. Therefore, no signal of extra dimensions is found and limits are set. Table 5.1 presents the event counts in different diphoton invariant mass ranges. The uncertainties in the backgrounds come from 20% photon fake rate systematic uncertainty. In the signal region, $m_{gg} > 500$ GeV, the predicted SM background is 0.303 ± 0.066 and no event is observed. The irreducible SM diphoton background is dominant in this signal region. The kinematic variables of the diphoton system are plotted in Figures 5.2 and 5.3. The background estimates agree well with the number of observed events in those kinematic distributions.

Process	$60 < M_{\gamma\gamma} < 200$ GeV	$200 < M_{\gamma\gamma} < 500$ GeV	$500 < M_{\gamma\gamma}$ GeV
Dijets	70 ± 28	0.5 ± 0.2	0.0009 ± 0.0004
γ+Jets	145 ± 7	2.3 ± 0.3	0.016 ± 0.003
Diphotons	150 ± 35	6.2 ± 1.4	0.286 ± 0.066
Total Backgrounds	365 ± 49	9.0 ± 1.5	0.303 ± 0.066
Observed	428	12	0

Table 5.1: Data measurements and background expectations for reconstructed diphoton invariant mass ranges. Full systematic uncertainties have been included.

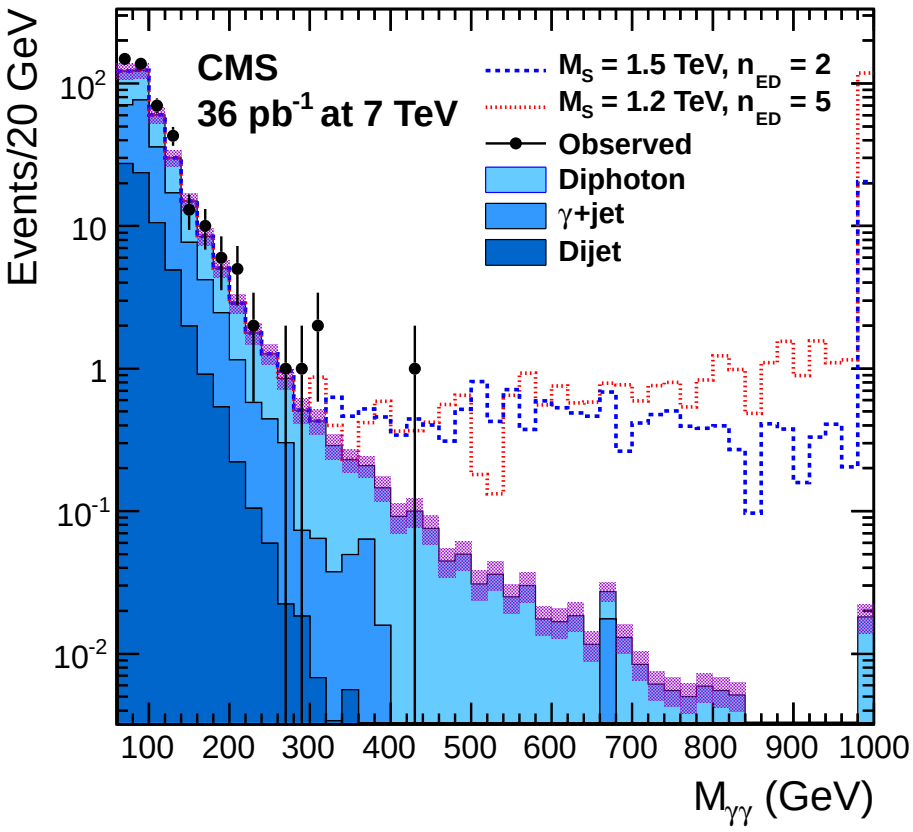

Figure 5.1: Data (points with error bars) and background expectations (filled solid histograms) as a function of the diphoton invariant mass. Photons are required to be isolated, with $E_T > 30$ GeV and $|\eta| < 1.4442$. Also shown with dashed lines the signal for two sets of model parameters.

5.2 Uncertainty

Table 5.2 summarizes the uncertainty of the analysis. The signal efficiency and signal K-factor uncertainty are described in Section 4.5 and Section 4.7.1. The uncertainty

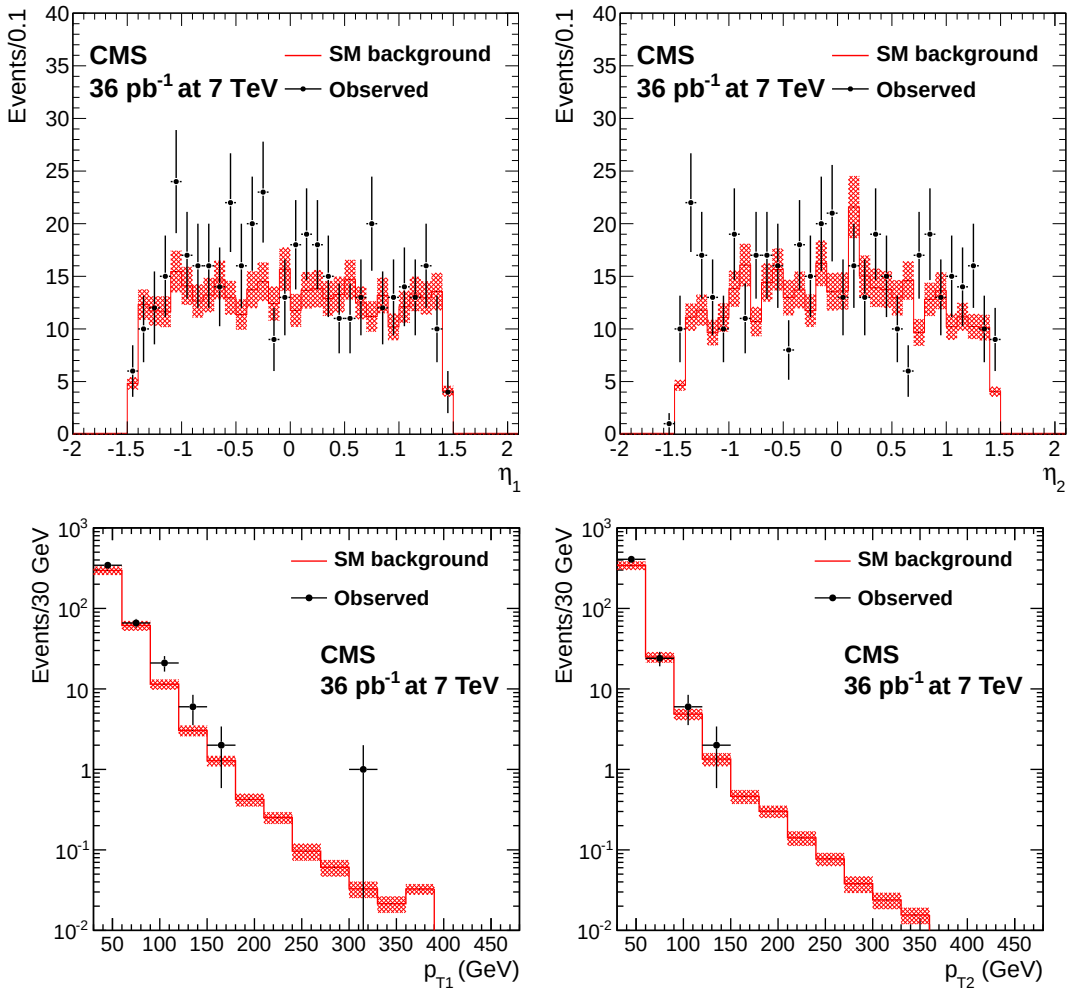

Figure 5.2: Distributions in η and E_T for the leading and sub-leading photons. Points with error bars represent data; the solid histogram corresponds to the expected background.

on the total background is calculated by adding individual background uncertainties in quadrature, except for those from the dijet and photon+jet backgrounds since they are both induced by the photon fake rate uncertainty. The relative combined background uncertainty is 21.8% which is dominated by the diphoton NLO K-factor uncertainty.

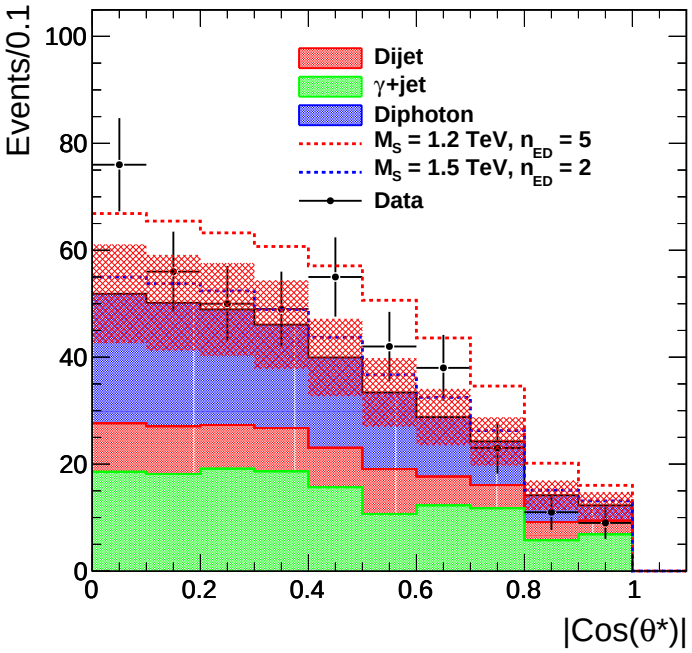

Figure 5.3: Scattering angle in c.o.m. frame of two photons

Table 5.2: Summary of systematic uncertainties.

	Central Value	Relative Uncertainty
Luminosity	36 pb $^{-1}$	4%
Background (Diphoton K factor)	0.30 Events	23%
Signal Efficiency	77.1%	5.4%
Signal K factor	1.3	7.7%
Acceptance uncertainty due to the PDF uncertainty	-	1.5%

5.3 Limit Setting Method

A standard Bayesian approach is used in the limit setting [69]. Suppose that there is a set of parameters ($\sigma\lambda$) involved in the experiment. σ is the parameter of interest, for example cross section and λ is a set of nuisance parameters, for example backgrounds, luminosity. The posterior density, $P(\sigma, \lambda|x)$, is related to the prior density, $\pi(\sigma, \lambda)$ and the model density, $P(x|\sigma, \lambda)$ by Bayes' theorem:

$$P(\sigma, \lambda|x) = \frac{P(x|\sigma, \lambda)\pi(\sigma, \lambda)}{\int\int P(x|\sigma, \lambda), \pi(\sigma, \lambda) d\lambda d\sigma} \tag{5.1}$$

where x is the observable. The prior density in Eq. 5.1 can be factorized as:

$$\pi(\sigma, \lambda) = \pi(\lambda|\sigma)\pi(\sigma) \tag{5.2}$$

Often, $\pi(\lambda|\sigma)$ is assumed to be $\pi(\lambda)$. The integral over all of the spaces of the nuisance parameters is performed and the posterior density in Eq. 5.1 is now a normalized function of σ. An upper limit, σ^{CL}, is found by integrating:

$$CL = \int_0^{\sigma^{CL}} L(\sigma|x)d\sigma \tag{5.3}$$

In the counting experiment presented in this dissertation, the observable is the number of observed events, n. The model density is conventional chosen as the Poisson likelihood of observing n events in data given a signal cross section times branching fraction times acceptance S, signal efficiency ε, the expected number of background events B, and an integrated luminosity $\mathcal{L}$:

$$P(n|S, \varepsilon, B, \mathcal{L}) = e^{-(B+\varepsilon S\mathcal{L})}\frac{(B + \varepsilon S\mathcal{L})^n}{n!}. \tag{5.4}$$

S is the parameter of interest and the nuisance parameter set includes ε, B and $\mathcal{L}$. A conventional flat prior is chosen for the cross section. The Lognormal functions with variance according to the uncertainties of the nuisance parameters are chosen as the priors of the nuisance parameters. The 95% upper limit on the signal cross section is found by solving:

$$\int_0^{S^{95}(n)} L(n|S)dS = 0.95. \tag{5.5}$$

5.4 Limits on the Large Extra Dimension Model

Using Table 5.2, the observed upper 95% CL limit on S is 0.118 pb. This limit is translated to the limit on the parameters of the ADD model, by the following technique. Since the effects of virtual graviton exchange interfere with the SM diphoton production, generally, we expect the overall cross section of the diphoton production from physics sources to have the following form:

$$\sigma_{\mathrm{ADD}} = \sigma_{\mathrm{SM}} + \eta_G\, \sigma_{\mathrm{int}} + \eta_G^2\, \sigma_{\mathrm{ED}}, \tag{5.6}$$

where η_G is the parameter specifying the strength of ED effects, as discussed in Section 1.5. After subtracting the σ_{SM} term, the cross section is parametrized as a bilinear form in the parameter η_G. For $n_{\mathrm{ED}} = 2$ case, η_G is not a constant, as it depends on the invariant mass of the diphoton pair. Therefore, in this case the signal cross section is parametrized with a smooth function of $1/M_S^4$. The limit on $1/M_S^4$ is found and further translated to the limit on the M_S. The expected

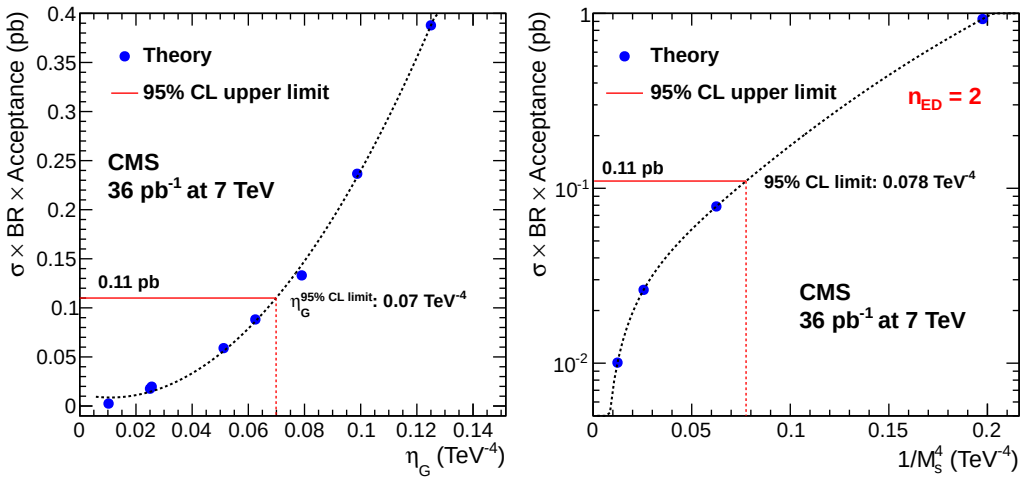

Figure 5.4: Signal cross section parameterization as a function of the strength of the LED, η_G (left) and as a function of $1/M_s^4$ for the $n_{ED} = 2$ case (right).

95% CL limit together with the signal cross section parametrization as a function

of η_G are shown on the left in Figure 5.4. The intersection of the cross section limit with the signal cross section curve determines the upper 95% CL limit on the parameter η_G. As seen from the plot, these limits are equal to $\eta_G^{95} = 0.070$ TeV^{-4} and $1/M_S^4(n = 2, 95\%) = 0.078$ TeV^{-4}. The translations to the lower limit on the fundamental Planck scale are done by using Eqs. (1.18). Table 5.3 shows those limits. The limits in the GRW convention [33] are identical to $n_{\mathrm{ED}} = 4$ HLZ limits; the limit in Hewett's convention with constructive interference is 1.73 TeV and is close to the HLZ limit for $n_{\mathrm{ED}} = 5$.

Table 5.3: Table of 95% CL limits on M_S (in TeV), as a function of the convention and number of ED. A comparison of the limits with a truncation of the production cross section above $\sqrt{\hat{s}} > M_S$ is also shown.

	HLZ					
	$n_{\mathrm{ED}} = 2$	$n_{\mathrm{ED}} = 3$	$n_{\mathrm{ED}} = 4$	$n_{\mathrm{ED}} = 5$	$n_{\mathrm{ED}} = 6$	$n_{\mathrm{ED}} = 7$
Full	1.89	2.31	1.94	1.76	1.63	1.55
Trunc.	1.80	2.23	1.84	1.63	1.46	1.31
	GWR	Hewett				
		Pos.	Neg.			
Full	1.94	1.74	1.71			
Trunc.	1.84	1.60	1.50			

From the theory construction, the LO signal cross section calculations become non-perturbative when $\hat{s}$ in the $2 \to 2$ process exceeds M_S^2. This effect is not taken into account in Sherpa cross section calculations used in this analysis, or in previous studies of this process at the Tevatron [70], where the effect is not expected to be important due to the lower machine energy. Since the energy of the LHC is significantly higher than the limits on M_S which can be set in this analysis, it is necessarily to take into account this effect by conservatively assuming that the signal cross section is zero for $\sqrt{\hat{s}} > M_S$. Under these assumptions the limits on M_S decrease by 5% for $n = 2$ (1.8 TeV) and 15% for $n = 7$ (1.31 TeV).

In addition to setting limits on a specific model of large extra dimensions, a

model-independent limit on any new physics mode which results in central, high p_T diphotons - either resonant or non-resonant (e.g. Kaluza-Klein gravitons in the Randall-Sundrum model [71]) is quoted. A 95% C.L. exclusion on the cross section times branching fraction times acceptance of 118 fb is set for diphoton pairs with $M_{\gamma\gamma} > 500$ GeV and the following kinematic requirements on each of the two photons: $p_T > 30$ GeV and $|\eta| < 1.4442$.

5.5 Conclusions

In conclusion, we have performed a search for large extra dimensions in the diphoton final state with a data sample collected in pp collisions at $\sqrt{s} = 7$ TeV corresponding to an integrated luminosity of 36 pb^{-1}. We optimize the signal selection to reach maximum sensitivity in a counting experiment in a one-sided mass window by selecting events with centrally produced photons ($|\eta| < 1.4442$) and large diphoton invariant mass ($m_{\gamma\gamma} > 500$ GeV). We estimate the SM backgrounds and compare with the observed data. Given the absence of an excess over the SM prediction, we set lower limits on the cutoff scale M_S in the range 1.6–2.3 TeV. These results extend the current limits reached at the Tevatron in all but the $n_{ED} = 2$ case.

While this analysis was being finalized, a phenomenological interpretation of the dijet angular distribution results from the CMS and ATLAS experiments appeared [72] and suggested even stronger limits on M_S. However, a dedicated experimental analysis and interpretation of the dijet data in the models with large extra dimensions has yet to be conducted.

Bibliography

[1] K. Nakamura et al. Review of Particle Physics. *J. Phys. G*, **37**:075021, 2010.

[2] G. Landsberg. Collider Searches for Extra Spatial Dimensions and Black Holes. *e-print: arXiv:0808.1867*, 2008.

[3] The LHC study group. The Large Hadron Collider Conceptual Design. *CERN-AC-95-05*, 1995.

[4] R. K. Ellis, W. L. Stirling, and B. R. Webber. *QCD and Collider Physics*. Cambridge University Press, 1996.

[5] J. Pumplin et al. New Generation of Parton Distributions with Uncertainties from Global QCD Analysis. *e-print arXiv:hep-ph/0201195*, 2002.

[6] A. Gupta, N. Mondal, and S. Raychaudhuri. Constraining Large Extra Dimensions Using Dilepton Data from the Tevatron Collider. *e-Print hep-ph/9904234*.

[7] D. J. Kapner et al. Tests of the Gravitational Inverse-Square Law below the Dark-Energy Length Scale. *Phys. Rev. Lett.*, **98**, 2007.

[8] Lyndon Evans and Philip Bryant (editors). LHC Machine. *JINST*, **S08001**, 2008.

[9] CMS Collaboration. Performance of the CMS Hadron Calorimeter with Cosmic Ray Muons and LHC Beam Data. *J. Instrum.*, **5**:T03012, 2010.

[10] CMS Collaboration. CMS Physics Technical Design Report Volume 1: Detector Performance and Software.

[11] CMS collaboration. Tracking and Primary Vertex Results in First 7 TeV Collisions. *CMS PAS TRK-10-005*, 2010.

[12] CMS collaboration. Performance of Muon Reconstruction and Identification in pp Collisions at $\sqrt{s}$ =7 TeV. *CMS PAS MUO-10-002*, 2010.

[13] CMS collaboration. Determination of the Jet Energy Scale in CMS with pp Collisions at *sqrts* = 7 TeV. *CMS PAS JME-10-010*, 2010.

[14] CMS collaboration. On Measuring Missing Transverse Energy with the CMS Detector in pp Collisions at $\sqrt{s} = 7$ TeV. *CMS PAPER JME-10-009*, 2010.

[15] E. Meschi, T. Monteiro, C. Seez, and P. Vikas. Electron Reconstruction in the CMS Electromagnetic Calorimeter. *CMS Note 2001/034*, 2001.

[16] CMS Collaboration. Photon Reconstruction and Identification at $\sqrt{s} = 7$ TeV. *CMS PAS EGM-10-005*, 2010.

[17] CMS Collaboration. Electron Reconstruction and Identification at $\sqrt{s} = 7TeV$. *CMS PAS EGM-10-004*, 2010.

[18] CMS collaboration. Electromagnetic Calorimeter Commissioning and First Results with 7 TeV Data. *CMS Note 2010/012*, 2010.

[19] Sheldon L. Glashow. Partial-symmetries of Weak Interactions. *Nucl. Phys.*, **22**:579, 1961.

[20] S. Weinberg. A Model of Leptons. *Phys. Rev. Lett.*, **19**:1264, 1967.

[21] A Salam. Elementary Particle Physics: Relativistic Groups and Analyticity. *N. Svartholm (Almqvist & Wiksell)*, 1968.

[22] G. 't Hooft. Renormalization of Massless Yang-Mills Fields. *Nucl. Phys.*, **33**:173, 1971.

[23] D. J. Gross and F. Wilczek. Ultraviolet Behavior of Non-Abelian Gauge Theories. *Phys. Rev. Lett.*, **30**:1343, 1973.

[24] H. D. Politzer. Reliable Perturbative Results for Strong Interactions. *Phys. Rev. Lett.*, **30**:1346, 1973.

[25] F. Abe et al. Observation of Top Quark Production in $p\overline{p}$ Collisions with the Collider Detector at Fermilab. *Phys. Rev. Lett.*, **74**:2626, 1995.

[26] S. Abachi et al. Observation of the Top Quark. *Phys. Rev. Lett.*, **74**:2632, 1995.

[27] K. Kodama et al. Observation of Tau Neutrino Interactions. *Phys. Lett. B*, **504**:218, 2001.

[28] Nakamura et al. (Particle Data Group). Review of Particle Physics, 2010-2011. Review of Particle Properties, 2010-2011. *J. Phys. G*, **37**:no. 7A, 075021, 2010.

[29] J. C. Collins, D. E. Soper, and G. Sterman. Factorization of Hard Processes in QCD. *e-print arXiv:hep-ph/0409313*, 2004.

[30] N. Arkani-Hamed, S. Dimopoulos, and G. Dvali. The Hierarchy Problem and New Dimensions at a Millimeter. *Phys. Lett. B*, **429**:263, 1998.

[31] J.C. Long and J.C. Price. *e-print arXiv:hep-ph/0303057v2*, 2003.

[32] G. Landsberg. Collider Searches for Extra Dimensions. *Preprint hep-ex/0412028*, 2004.

[33] G. Giudice, R. Rattazzi, and J. Wells. Quantum Gravity and Extra Dimensions at High-Energy Colliders. *Nucl. Phys.*, **B544**:3, 1999.

[34] J. Hewett. Indirect Collider Signals for Extra Dimensions. *Phys. Rev. Lett.*, **82**:4765, 1999.

[35] T. Han, J. Lykken, and R. Zhang. On Kaluza-Klein States from Large Extra Dimensions. *Phys. Rev. D*, **59**:105006, 1999.

[36] E. G. Adelberger. Sub-mm Tests of the Gravitational Inverse-square Law. *e-Print hep-ex/0202008*, 2002.

[37] S. Cullen and M. Perelstein. . *Phys. Rev. Lett.*, **83**:268, 1999.

[38] S.Ask. Search For Extra Dimensions At LEP. *e-print: arXiv:hep-ex/0410004*, 2004.

[39] CFF Collaboration. 2007. `http://www-cdf.fnal.gov/physics/exotic/r2a/20071213.gammamet/LonelyPhotons/photonmet.html`.

[40] D0 Collaboration. D0 Note 5729-CONF. 2008. `http://www-d0.fnal.gov/Run2Physics/WWW/results/prelim/NP/N63/N63.pdf`.

[41] CDF Collaboration. 2007. `http://www-cdf.fnal.gov/physics/exotic/r2a/20070322.monojet/public/ykk.html`.

[42] D0 Collaboration. to be submitted to Phys. Rev. Lett.; O.Stelzer-Chilton, talk at the 34th Int. Conf. on High Energy Physics, ICHEP 08. 2008. `http://www.hep.upenn.edu/ichep08/talks/misc/schedule`.

[43] D0 Collaboration. D0 Note 5729-CONF. 2008. `http://www-d0.fnal.gov/Run2Physics/WWW/results/prelim/QCD/Q11/Q11.pdf`.

[44] CMS collaboration. The CMS Experiment at the CERN LHC. *JINST 3*, **S08006**.

[45] CMS Collaboration. Electromagnetic Calorimeter Calibration with 7 TeV data. *CMS PAS EGM-10-003*, 2010.

[46] CMS Collaboration. CMS The TriDAS Project Technical Design Report, Volume 1: The Trigger Systems. *CERN/LHCC 2000-38*, 2000.

[47] CMS collaboration. Track Reconstruction in the CMS Tracker. *CMS PAS TRK-09-001*, 2009.

[48] R. Fruhwirthu. Application of Kalman Filtering to Track and Vertex Fitting. *Nucl. Instrum. Meth.*, **A262**:444, 1987.

[49] Tracking and b Tagging POGs. Tracking and Vertexing Results from First Collisions. *CMS AN-2010/055*, 2010".

[50] R. Fruewirth et al. Adaptive Vertex Fitting. *CMS Note 2007/008*, 2007.

[51] CMS collaboration. Performance of Jet Algorithms in CMS. *CMS PAS JME-07-003*, 2007.

[52] G. C. Blazey et al. Run II Jet Physics: Proceedings of the Run II QCD and Weak Boson Physics Workshop. *hep-ex 0005012*, 2000.

[53] M. Cacciari et al. The Anti-kt jet Clustering Algorithm. *JHEP*, **0804:063**, 2008.

[54] CMS collaboration. Jet Plus Tracks Algorithm for Calorimeter Jet Energy Corrections in CMS. *CMS PAS JME-09-002*, 2009.

[55] CMS collaboration.

[56] CMS collaboration. Commissioning of TrackJets in pp Collisions at $\sqrt{s} = 7$ TeV. *CMS PAS JME-10-006*, 2010.

[57] CMS collaboration. Jet Performance in pp Collisions at $\sqrt{s} = 7$ TeV. *CMS PAS JME-10-003*, 2010.

[58] S. Esen et al. Missing Transverse Energy Performance in CMS. *CMS AN-2007/041*, 2007.

[59] CMS collaboration. Performance of Missing Transverse Energy Using Calorimeter and Tracks in CMS. *CMS PAS JME-09-006*, 2009.

[60] N. Marinelli. Track Finding and Identification of Converted Photons. *CMS NOTE 2006/005*, 2006.

[61] W. Adam et al. Electron Reconstruction in CMS. *CMS AN-2009/164*, 2009.

[62] W. Adam et al. Reconstruction of Electrons with the Gaussian-Sum Filter in the CMS Tracker at the LHC. *CMS NOTE 2005/001*, 2005.

[63] T. Sjostrand, S. Mrenna, and P. Skands. PYTHIA 6.4 Physics and Manual. *JHEP*, **05**:26, arXiv:0603175, 2006.

[64] T. Sjostrand, S. Mrenna, and P. Skands.

[65] T. Gleisberg, F. Krauss, K. Matchev, A. Schalicke, S. Schumann, and G. Soff. Helicity Formalism for Spin-2 Particles. *e-print: arXiv:hep-ph/0306182*, 2003.

[66] Matteo Sani. Photon Efficiency Measurements Using Tag and Probe. *CMS AN-2010/292*, 2010.

[67] A. Askew et al. A First Search for General Gauge Mediated SUSY. *CMS Note*, 2010.

[68] T. Binoth et al. A Full Next-to-leading Order Study of Direct Photon Pair Production in Hadronic Collisions. *Eur. Phys. J.*, **C16**:311, 2000.

[69] I. Bertram et al. A Recipe for the Construction of Confidence Limits. *FERMILAB-TM-2104*, 2000.

[70] D0 collaboration. Search for Large Extra Spatial Dimensions in the Dielectron and Diphoton Channels in $p\overline{p}$ Collisions at $\sqrt{s} = 1.96$ TeV. *Phys. Rev. Lett.*, **102**:051601, 2009.

[71] L. Randall and R. Sundrum. . *Phys. Rev. Lett.*, **83**:3370 and ibid (1999) 4690, 1999.

[72] R. Franceschini et al. LHC bounds on large extra dimensions. *e-print: arXiv:1101.4919*, 2011.